Insights into fluid transport mechanisms at White Island from analysis of coupled very long-period (VLP), long-period (LP) and high-frequency (HF) earthquakes

A.D. Jolly[1], I Lokmer[2], J. Thun[2,3], J. Salichon[1], B. Fry[1], L. Chardot[4]

[1]GNS Science, 1 Fairway Drive, Avalon, Lower Hutt, New Zealand

a.jolly@gns.cri.nz

[2]University College Dublin, Belfield, Dublin 4, Ireland

[3]Dublin Institute for Advanced Studies, 5 Merrion Square, Dublin 2, Ireland

[4]GNS Science, Wairakei Research Centre, 114 Karetoto Rd. Taupo, New Zealand

Abstract: The August 2012 to October 2013 White Island unrest sequence included 5 explosive volcanic eruptions and emplacement of a small dome. These events were linked to an overall increase in SO_2 and H_2S gas flux and RSAM seismic tremor which began in late 2011. Prior to this unrest, a small swarm of 25 events was observed on 19-21 August 2011 and captured on a temporary seismic array including 14 broadband sensors. Each event comprised coupled pulses having distinct high frequency (HF =2-5 Hz), long-period (LP = 0.5-1.1 Hz) and very long period (VLP = 0.04-0.125 Hz or 8-25 s) earthquakes.

For each coupled event, we compute the source locations, origin times and related uncertainties by application of standard arrival time locations for the HF earthquakes and waveform semblance for the LP and VLP earthquakes. Results suggest that the events are centred beneath the active vent at depths generally less than 1.5 km. The HF and LP earthquakes have shallow depths (less than1 km), while VLP have slightly deeper source locations (0.8-1.5 km). Emergent onsets for LP and VLP sources make an analysis of the absolute origin times problematic but waveform matching of VLP to LP and HF components suggests that the main VLP pulse precedes the HF and LP source processes.

Waveform inversion for the VLP source is consistent with the rupture of a high angle East-West oriented crack opening either in a purely tensile or shear-tensile manner. The moment of the isotropic component is estimated at 1.2×10^{12} Nm and the corresponding volumetric change is about 145-450 m^3.

Results are interpreted as an upward migration of fluids which first excite the VLP from a high angle crack in the magma carapace followed by the excitation of LP and HF source processes in the overlying hydrothermal system.

Keywords: Volcano seismology; Waveform inversion; Volcanic gases; Numerical modelling

1. Introduction

The nature and character of volcanic plumbing systems may be elucidated from a range of observations including gas geochemistry (Christenson and Wood, 1993; Francis et al, 1998; Burton et al, 2000;Werner et al., 2008), seismology (Chouet et al., 1996; Neuberg et al., 1998; Kumagai et al., 2003; Bean et al., 2014), geophysics (Ingham, 2009; Legas et al., 2009) and an interpretation of the chemistry and character of the eruptive products (e.g., Houghton and Nairn, 1991;Valentine and White, 1991; Kilgour et al., 2010; Lube et al., 2014).

White Island volcano (Fig 1) is a frequently active composite cone with a deeply excavated central crater. It is a well-studied island volcanic system thought to include an upper to mid-crustal magma chamber (Cole et al., 2000; Werner et al., 2008), a shallow hydrothermal system (e.g., Fournier and Chardot, 2012; Chardot et al., 2015, Heap, 2015) and having pervasive magmatic degassing (Werner et al., 2008) which suggests the presence of shallow magma over periods of decades and longer. The long term degassing trend may indicate the presence of a shallow convecting magma system (e.g., Kazahiya et al., 1994; Stevenson and Blake, 1998) or alternatively to the pervasive injection and crystallisation of magma to shallow depth (e.g., Cole et al., 2000). For the former, it is uncertain if convection is possible for degassed and viscous magma. For the latter, it is uncertain if magma injection rates can yield sufficient degassing without attendant deformation associated intrusion. Evidence for deeper magma (18-22 km) at White Island is inferred from receiver functions of teleseismic waves (Park and Kim, 2014).

White Island volcano produces a wide range of seismic activity, including tremor and discrete LP activity (Sherburn et al., 1998) and volcano-tectonic activity (Nishi et al., 1996), with frequencies >1 Hz, which are here denoted as high frequency (HF) activity to specifically

remove reference to rock failure processes and to generalise the event types to other possible genetic processes. This range of activity was described in detail from data collected during an earlier dense array deployment to White Island in 1992 (Nishi et al., 1996). In addition to these previously identified event types, here we note for the first time that very long-period (VLP) earthquakes (e.g., Kawakatsu et al., 1992; Neuberg et al., 1994) are also present at White Island. The prior VLPs occurred infrequently, were characterised by wave periods of ~8-25 s and were first observed with the establishment of broad-band seismic monitoring in 2007. Before this period, seismicity was monitored using short-period seismic sensors and VLP activity may have occurred but remained undetected.

In the 14 month period from 5 August 2012 to 11 October 2013 White Island experienced 5 ash and steam eruptions (Chardot et al., 2015), numerous small scale mud and ash eruptions (Jolly et al., 2016) and the extrusion of a small lava dome sometime in September-November 2013 (Fig 2). The ash and steam eruptions were recorded on the WIZ seismic station which was joined by station WSRZ in April 2013. Before the eruption sequence GNS Science deployed 14 temporary broadband seismic sensors for approximately 6 months (Fig 2). The deployment period was characterised by mostly low level activity, however, twenty-five mixed frequency events including very long period (VLP), long-period (LP) and high frequency (HF) components were observed on 19-21 August 2011 (Fig 3 and 4). This paper focuses on the 19-21 August activity which, in hindsight, may have been the first precursor to the 2012-2013 unrest periods.

The coupled events provide a valuable opportunity to examine the source processes that may produce such seismicity in volcanic regions owed to their close temporal and spatial relationship by examination of a small sequence of coupled HF, LP and VLP events. We focus on constraining the timing and spatial relationship between the coupled events through the use of specific seismological tools. For the HF component we rely on arrival time

location methods (e.g., Lee et al., 1972) to obtain event locations from a well constrained upper crustal velocity model (Jolly et al., 2013). For the LP and VLP components we utilised a waveform semblance approach (e.g., Kawakatsu et al, 1999; Almendros et al., 2002) to constrain their location. The relative timing of each coupled event is examined by analysis of waveform onsets and from waveform matching techniques.

2. Data

Coupled HF, LP and VLP events were captured on a temporary dense array deployment of 13 broad-band sensors that were operating between June and November 2011. The temporary array comprised Guralp 6T and 40T sensors and 24 bit Nanometrics Taurus digitisers which recorded continuously at a sampling rate of 100 Hz. The temporary network joined a single permanent station WIZ (see Fig 1) equipped with a Guralp 3ESP sensor with a 24 bit Quanterra digitiser that also sampled at 100 Hz. All sensors had flat response characteristics from either 30 or 60 seconds to the Nyquist frequency (50 Hz) and were processed as appropriate for the subsequent set of analysis.

The 6-month deployment period was remarkably quiet in terms of local seismicity, including low level tremor and very little discrete volcanic earthquake activity. Surface features at this time were also muted with no notable surface activity. The 19-21 August swarm event was initially recognised by visual inspection of the real time data on station WIZ. An STA/LTA algorithm was applied to the entire 6-month period to extract relevant low frequency events. This procedure highlighted 25 events recorded from 19-21 August and other triggered events that had mostly teleseismic origin.

As a first step in processing, we examined a regional event to confirm the polarity of stations and components in the temporary and permanent network. We also identified failed components (WI02, E-component) and sites with poor long period response characteristics (WI04, both horizontal components), an effect that may be associated with the installation rather than a specific site effect. Initial examination of the August 19-21 sequence revealed coupled VLP, LP and HF frequency components for each event (see Fig 3 event 16 and 17 for example).

Analysis of the frequency characteristics of a good signal to noise example event (Fig 4A) allowed an overview of the specific spectral characteristics of the earthquake sequence with HF earthquakes having spectral bands from 2-5 Hz, LP frequencies from 0.5 to 1.1 Hz, and VLP having 0.03 to 0.125 Hz (Fig 4B). The frequency content of the HF events is conspicuous when compared to the broader spectrum associated with classical rock failure volcano-tectonic (VT) earthquakes, an observation which may reflect source process or high levels of noise at White Island. This is examined further in the discussion section. The zero-phase band passed waveforms suggest that the main VLP onset precedes the HF and LP event by a few seconds (Fig 4C), an observation that is also seen in other events of the sequence (Fig 3). This observation also is consistently seen when a strictly causal filter is applied, which implies that it is not an artefact of the zero-phase filters used in most of our analysis. In addition, a weaker VLP onset at about 30 seconds is seen in high signal to noise examples (e.g., Fig 3, events 17, 19, 20). The features in individual events are also seen from stacked unfiltered waveforms (analysis not shown) confirming that the VLP indeed precedes the LP/HF activity.

To understand the temporal and spatial patterns for the sequence, we utilised classic waveform semblance (Kawakatsu et al, 2000) to locate VLP (Table 1) and LP (Table 2) events and a standard arrival-time approach to locate HF sources (Table 3). We also

performed full waveform inversion for the moment-tensor the and the time-history of the VLP source. All the outlined methods rely on the knowledge of velocity structure which we discuss next.

3. Shallow velocity structure at White Island

The shallow velocity structure at White Island was perviously constrained from an active source experiment conducted in November 2011 at the end of the dense array deployment (Jolly et. al., 2013). This work found that the unconsolidated tephra within the shallow crater floor had low velocities of approximately 1.2 km/s while the crater walls had velocities of 2.2 km/s. Ray paths from the active sources only propagated to depths of a few hundred m below the surface however and deeper velocities were not sampled. To verify the active source results and sample deeper portions of the volcanic system, we applied a noise interferometry approach using the temporary dense array data. We analysed a linear array of temporary seismometers extending in a northwest-southeast direction paralleling the valley floor. These data were supplemented by a broadband station (WI05) on the north-western flank of the edifice to derive a shear-wave velocity model of the upper ~1.0 km of the crater area of White Island. The dense crater floor array had a length of about 0.8 km (see Jolly et al., 2013, their Fig 1). The linear aperture is further increased to about 1.5 km with the addition of the north western station (WI05). We use noise interferometry to generate dispersion curves between about 0.5 and 5 Hz (as in Stehly et al, 2009; Fry et al, 2010). This wide bandwidth of dispersion observations is obtained by generating a single composite dispersion curve, selecting the frequency range contribution of each station pair according to its inter-station distance. We aim to investigate the uppermost km of the crater floor so we first decimated the data to 10 Hz. Other pre-processing steps include removing the instrument response and

157 the mean from the seismic data, and whitening the signal to remove the spectral peaks of the
158 spectrum to satisfy the requirement of equipartition for ambient-noise analysis. The latter is
159 necessary to assume that the cross-correlation function equals the Green's function between
160 two stations.
161 We performed a time-domain cross correlation of station pair per day and stacked the data
162 over the whole period, which is equivalent to combining the effects of sources located at
163 different azimuths towards equipartition. A group velocity was then computed for each
164 station pair, after multiple filtering to isolate the fundamental mode. Rayleigh waves are
165 dispersive, so their velocity depends on the frequency. We therefore extracted the phase
166 velocity for each station pair and each frequency and obtained a dispersion curve with a
167 standard deviation by summation. Since the Rayleigh wave velocity is a function of *Vp, Vs,*
168 density and the layer thickness, this dispersion curve was finally inverted to obtain a 1-D *Vp,*
169 *Vs* and density profiles. We invert the resulting dispersion curves with the geopsy (Wathelet,
170 2008) software to obtain a layered 1D V_s model. Our results allow us to generate a multi-
171 resolution model with ~5 m vertical resolution in the upper 20 m and ~200 m resolution at 1
172 km depth. We define interfaces at ~4 m, ~80 m, and ~1100 m. Below 1100 m, we define V_s
173 ~ 1.225 km/s and V_p ~ 3.25 km/s. Results suggest that on average, the crust beneath the
174 volcano experiences a strong shallow velocity change at about 90 m in the central crater
175 where V_P ~ 1.2 km/s underlain by a ~1 km layer with V_P ~ 2.4 km/s. These results are
176 consistent with velocity estimates obtained from the active source experiment (Jolly et al.,
177 2012) with low velocities ascribed to unconsolidated tephra and higher velocities ascribed to
178 the underlying consolidated volcanic rocks. Interestingly, the V_p/V_s ratio in the region is
179 relatively high at about 1.95, suggesting the presence of at least a small amount of volatiles
180 and hot rock in the uppermost km (Fig 5).

Because the active source and dispersion curve results match closely, with only ~0.2 km/s difference for the upper km of the analysis, we completed our analysis of the swarm locations using a uniform velocity of both 2.2 km/s and 2.4 km/s as reasonable range of velocity model uncertainties. Results of the location analysis and the reasonable alternative models are discussed next.

4. Source locations

4.1 Waveform semblance

We used the waveform semblance approach as detailed in Kawakastu et al. (2000), and subsequently utilised by Almendros et al. (2002) and Almendros and Chouet (2013) for the analysis of LP and VLP components which are in turn derived from the pioneering work of Neidel and Tarner (1971). Coherency amongst seismograms can generally be measured using:

$$S = \sum_{j=1}^{L}\left(\sum_{i=1}^{N} u_{i,j(i)}\right)^2 \Big/ N\sum_{j=1}^{L}\sum_{i=1}^{N} u_{i,j(i)}^2 \quad , \qquad (1)$$

where L is the length of the seismogram, N is the number of stations and $u_{i,j(i)} \equiv u_i(t_i + j\Delta t)$ is a seismogram of the ith station at the $j(i)$th time sample at the start time t_i.

Waveform coherence implies that the stationary isotropically radiating point-source imparts seismic energy to all stations as compressive body waves that may be rectified into a linear particle motion (Kawakatsu et. al, 2000). In the radial component (the direction of a station from the source) the seismogram particle motion is given by $u_{i,j(i)} \equiv R_{i,j(i)}$. Different stations

have different source station travel-times and adjustments for these time delays (t_i) should increase the radial components waveform coherence. There may also be mutually perpendicular components $H_{i,j(i)}$ and $V_{i,j(i)}$, which for an isotropic radiating source having well behaved ray paths, should have negligible contributions. The waveform semblance may be incorporated to emphasise the radial excitation from the isotropic source and penalise departures from rectilinear behaviour via the following equation (Kawakatsu et al., 2000):

$$S_3 = \frac{1}{D}\sum_{j=1}^{L}\left\{\left(\sum_{i=1}^{N} R_{i,j(i)}\right)^2 - N\left(\sum_{i=1}^{N} V_{i,j(i)}^2\right) - N\left(\sum_{i=1}^{N} H_{i,j(i)}^2\right)\right\}, \quad (2)$$

where V is the component in the direction perpendicular to R within the vertical plane which contains both source and receiver, and H is in the horizontal component perpendicular to both R and V (V is generally not vertical). L is the number of time samples and N is the number of stations. We take the scaling factor D as:

$$D = N\sum_{j=1}^{L}\sum_{i=1}^{N} R_{i,j(i)}^2. \quad (3)$$

S_3 measures the rectilinearity of particle motion pointing via the signal coherency in the radial direction. As in Kawakatsu et al., (2000) we normalise each seismogram so that the RMS amplitude of each signal at each station becomes unity:

$$RMS_i^2 = \frac{1}{L}\sum_{j=1}^{L}(R_{i,j(i)}^2 + V_{i,j(i)}^2 + H_{i,j(i)}^2) = 1, \quad (4)$$

which removes amplitude information from the original seismograms giving equal weight to each station during the coherence computation.

In practice, for each event, we compute the waveform semblance within a grid search of the target volume. We first compute a search over a 3 km grid centred on the crater lake and from sea level to 3 km below sea level at 100 m spacing. In our case, we search to a depth of 3 km as this would be just beyond the lower limit of resolution given the aperture of the dense array deployment. At each point we compute the source to station distance, azimuth and incidence angle and rotate the *N*, *E*, *Z* seismograms for each station into *R*, *H* and *V* components having an appropriate travel-time-delay based on the independently determined velocity model. Results are normalised using Eq (4) and the waveform semblance is computed with Eq. (2). For this formulation, the waveform semblance varies between -1 and 1, with 1 indicating perfect coherence without penalty from the *H* and *V* components. After determining the best fit semblance in the coarse grid search, we re-computed the semblance within a 20 m grid spacing within a 200x200x200 m search volume centred on the best fit coarse solution. Before proceeding to the location of LP and VLP sources using the semblance method, we first show the performance and error analysis using synthetic data.

4.2 Synthetic test of waveform semblance

To obtain an improved understanding of the limitations and accuracy of the method, we compute synthetic seismograms and then determined their source location in a blind test

using the waveform semblance technique described above. The synthetic seismograms are computed with the open source spectral-element method (SEM) code EFISPEC3D (http://efispec.free.fr; De Martin, 2011). The numerical domain is based on a 10 x 10 x 7 km^3 rectangular cuboid (boundary conditions: free surface at the top, absorbing boundaries at the other 5 surfaces). The surface is then altered to reflect the local topography of White Island, using a combination of a Digital Elevation Model (DEM) for the island and a bathymetry model for the surrounding seabed (Prasetya, and Wang, 2011**)**. Water can currently not be accounted for in EFISPEC3D, but is expected to have minor effects on the waveforms computed for this test. An example of the computational setup is shown in Fig 6.

The receivers are located at the free surface, at positions corresponding to the receivers in the field experiment. The synthetic sources are located at a horizontal position (E 2880132 m; N 6400282 m in depths of 1.0 km and 2.0 km below sea level, respectively. For the source mechanism we use explosive sources, horizontal tensile cracks and steep oblique tensile cracks striking at 25° from North and dipping at 75°. As the source time function (STF) we use a 1 Hz low-pass filtered VLP displacement waveform from an event recorded at WIZ station. This is justified by the very long wavelength for the waveforms which are dominated by near to mid-field terms; the intermediate-field displacement term is directly proportional to the time-history in the source, and the near-field term, for a small P to S difference (relatively to the dominant period of the waveform) has the same shape. Moreover, the VLP signals are strikingly similar between different stations, so it is fully justified to use the WIZ station, which has good signal-to-noise characteristics. Two different velocity models are used: (i) homogeneous (V_P = 2.3 km/s, V_S = 1.328 km/s, ρ = 2160 kg/m^3) and (ii) layered model described in Section 3.

For the blind test, we generate seismograms for 8 different combinations of velocity models, mechanisms and depths, listed in Table 4. Four of the synthetic examples include explosive sources, two examples model horizontal tensile cracks, and 2 models have oblique tensile cracks. In addition, two of the examples include a superposition of typical White Island background noise.

An example of relocation using the semblance approach from Section 4.1, is shown in Fig 7. The relocation of a simple isotropic source is within 100 m of the synthetic computation with differences possibly owed to minor uncertainties in the DEM, and topographic effects. The accurate recovery of the isotropic source then provides a basis for an examination of uncertainties associated with the introduction of noise, velocity structure and the departure from isotropic source geometries. Alternate input velocities (Section 3) were found to produce only minor changes in the retrieved semblance locations of less than 100 m.

Results of the 8 cases show the following general trends: 1) explosive sources were well recovered (error less than 200 m) by the waveform semblance, 2) horizontal tensile cracks tend to yield consistently shallow solutions and the introduction of unknown layered velocity structure tends to increase the effect, 3) oblique high angle tensile cracks tend to produce poor semblance values and significant departures from the true source location (> 200 m lateral mis-location and ~100 m depth mis-location) and the location misfits are larger (~1000 m lateral mis-location) if the noise levels are high. 4) noise levels generally increase the misfit between true location and computed location and decrease semblance: a result that is also apparent in the natural data (Section 4.3). In general, these tests suggest that while near vertical crack geometries yield very high misfit values with the known synthetic location, these effects can be identified because the semblance will be low for a dense seismic network. We note however that sparse networks may lead to erroneously high semblance values due to undersampling of the non-uniform source focal sphere. In general, we find that

292 the location error increases for the sources with strongly non-isotropic radiation pattern
293 across the network (such as a vertical crack).

294

295 **4.3 Location of LP and VLP sources**

296 After confirming the accuracy of the method using a variety of synthetic sources, we next
297 applied the results to each of the 25 events for zero-phase offset filtered seismograms (Fig. 4)
298 for both LP and VLP source components. As noted in Section 2, the onset of the VLP occurs
299 ~30 seconds prior to the main VLP/LP and HF pulses. In our case, the semblance analysis is
300 completed on the band pass filtered main phase and not the preceding low amplitude VLP
301 signal. An example of the particle motion results at the best fit location for event 17 is
302 shown for a VLP and LP event (Fig 8, Fig 9). This event was selected because it had good
303 signal to noise and VLP semblance but was not the 'best' example (as measured by
304 semblance), hence more representative of a good example event.

305 The map view particle motions (Fig 8A) for the VLP event show that a source located south
306 of the summit is reasonable, but there are notable and systematic polarisation deflections
307 from the best fit source position. Note specifically in this example the apparent deflection of
308 WI08 and WI09 which contributes to a location south of the central crater. This is possibly
309 owed to a significant contribution of a non-isotropic source mechanism and mixing of P- and
310 S-phases (for details about source mechanism see Section 5). The associated depth-section
311 particle motions (Fig 8B), where each particle motion is rotated from its azimuth projection,
312 show that stations closer to the source have high incidence angles and further stations have
313 shallower incidence. This result is expected for a highly coherent semblance result from a
314 mostly uniform source.

315 In contrast, the LP example for the same coupled event 17 (Fig 9) yields significant
316 discrepancies between particle motions across the network. In this case, subsets of stations
317 have very different particle motion results and the weakly coherent waveform semblance
318 estimate is very low (see negative semblance values Table 2).

319 It has been standard practice to compute these error bounds based on a semblance error limit
320 within the search volume (Kawakatsu, 2000, Almendros 2002, Almendros 2003). Almendros
321 (2003) discusses a criterion semblance level S_L=(1 - δS)S_{MAX} , based on the signal-to-noise
322 ratio (*SNR*) which may be used to establish the error bounds (δS) for a semblance location.
323 In that case, the error bounds were determined empirically from synthetic data including a
324 known *SNR*.

325 $$\delta S = 0.062\, SNR^{-1.54}$$

326 (5)

327 In our case, the semblance is noted to vary strongly at low SNR and stabilise for SNR > 3
328 (Fig 10). The empirical relation yields error limits of about 1% in our case which may not be
329 appropriate for White Island. Instead, for VLP source locations we used an error limit of 2%
330 of maximum semblance, which yield lateral errors about the same as the mis-locations found
331 in synthetic tests for explosions and horizontal tensile cracks. For LP events, having
332 consistently lower semblance values, we used a semblance error limit of 50% of maximum
333 semblance, which yielded lateral errors similar to the vertical crack synthetics. This approach
334 should offer reasonable first order estimates of the location uncertainty.

335 Next we examine the 25 events using the same semblance approach for individual events.
336 From this analysis, we obtain the range of locations and associated error bounds for the 25
337 coupled events (Fig 11). For the VLP events, we find that locations are distributed over the

338 southern crater margin and at an average depth of ~1 km. Formal errors from the analysis of
339 synthetic data yield lateral errors of ~+/-150 m and depth errors of ~200 m. However, given
340 the uncertainties in velocity structure and possible departures from the point source
341 assumption, it is possible that VLP sources actually originate from the same source position.
342 The distribution of locations is somewhat larger than our established error bounds, however,
343 with lateral errors of about 800 m E-W, 500 m N-S and 500 m in depth. We note that the LP
344 sources for the same earthquake sequence have very different location distribution and error
345 bounds. LP events tend to be distributed over the northern margin of the crater (Fig 11)
346 having formal errors of about +/- 300 m laterally and ~1000 m vertically. Shallower LP
347 events have unconstrained errors whose formal error limits are beyond the search grid. The
348 distribution of earthquake locations is more tightly clustered laterally (within ~300 m) but has
349 a wide range of depths (from the surface to 900 m depth). Semblance locations for VLP and
350 LP events are summarized in Tables 1 and 2. We note that particle motions may be
351 significantly distorted due to topographic gradients that may be corrected if the gradient is
352 well determined (Neuberg and Pointer, 2001). In our case VLP wavelengths are much longer
353 than the wavelength of the topography and the distortions or corrections would be difficult to
354 determine.

355

356 **4.4 High-frequency (HF) earthquake location**

357 The 25 HF earthquakes included significant variation in the signal-to-noise ratio from event
358 to event which negatively affected the ability to pick arrival times and determine the location.
359 However, detailed examination of manually picked arrival times for *P* phases produced a
360 subset of 8 of the 25 events which could be located. *S* phases could not be discriminated
361 (Fig. 4). For these events locations were computed using a uniform half-space model having

2.2 km/s (consistent with the model derived in Section 3) using the HYPO71 location algorithm (Lee et al., 1972). We note that the half space model used here is consistent with the model used to compute LP and VLP solutions.

Locations were initially attempted using a range of alternate models and layered models which produced substantial variation in hypocentre location. The active source model (V_p = 2.2 km/s) yielded locations beneath the central crater and depth of ~400-500 m. The modestly higher velocities derived from the Rayleigh wave cross-correlation results yielded slightly shallower (~100 m) HF earthquake locations. Location results shown in Fig 11 are summarised in Table 3.

5. Source inversion

The prior analysis provides well constrained VLP source locations which can now be used to develop an understanding of the underlying source process. Hence, we proceed next to the waveform inversion for VLP source excitation. Although many VLP inversions performed so far (e.g., Ohminato et al., 1998; Nishimura et al., 2000; Hidayat et al., 2002; Chouet et al., 2003; Kumagai et al., 2003; Chouet et al., 2005; Ohminato, 2006; Aster et al., 2008; Molina et al., 2008; Waite et al, 2008; Dawson et al., 2011; Chouet and Dawson, 2011; Maeda and Takeo., 2011; Haney et al., 2012; Maeda et al., 2015a) differ in the inferred source geometries and interpretation (dykes, sills, connected chambers, dyke-sill composites), they suggest that the VLP activity represents the elastic response of the rocks in the volcanic plumbing system to mass transport inside a volcano. While numerous studies deal with VLP events which are directly related to volcanic explosions (e.g., Chouet et al, 2003; Aster et al., 2008; Maeda et al., 2015b), there are also reports of VLP activity during periods of eruptive quiescence (e.g., Saccorotti et al., 2007; Zuccarello et al., 2013).

Due to the very long wavelengths (~20–75 km in this study), VLP signals are relatively insensitive to strong structural heterogeneities present inside volcanoes. This means that distortions of the wavefield from path effects are minimal, enhancing our ability to reliably invert for the source mechanisms of these signals. On the contrary, LP signals with the wavelengths of only several kilometres are severely distorted by both heterogeneity and pronounced volcano topography (e.g., Neuberg and Pointer, 2000), hence their inversion can be challenging. Bean et al. (2008) and Trovato et al. (2016) demonstrate through a suite of synthetic tests that an inaccurate shallow velocity model has a detrimental effect on moment-tensor solutions of LP sources. Both studies point out that a good waveform fit does not necessarily imply a correctly recovered source mechanism. In particular, Trovato et al. (2016) suggest moving towards lower frequencies (if available) and/or using the tilt in the inversions. In addition to these complications, the signals recorded on White Island, when filtered in the LP frequency band, are heavily contaminated by noise, largely caused by oceanic microseisms and wind, which renders them exceptionally challenging for source inversion. For the outlined reasons, we only perform the source inversion of VLP events.

5.1 Method

The seismic ground motion observed at the surface is a convolution of the source (moment tensor) with the path effect (Green's functions, GFs). The relationship between the source components and the surface displacements can be expressed as a linear equation:

$$\mathbf{u} = \mathbf{G}\mathbf{m}, \tag{6}$$

where **u** is the data vector containing recorded seismograms, the matrix **G** contains the GFs for all stations and components and the vector **m** contains the moment tensor components. The weighted least squares solution of this equation can be written as (Menke, 1984):

$$\mathbf{m}^{\mathrm{est}} = (\mathbf{G}^{\mathrm{T}}\mathbf{W}\mathbf{G})^{-1}\mathbf{G}^{\mathrm{T}}\mathbf{W}\mathbf{u}, \tag{7}$$

where **W** is a vector of weights for all data traces. The synthetic seismograms corresponding to this solution are obtained by convolving the solution $\mathbf{m}^{\mathbf{est}}$ with the GFs (Eq. 6). The residual *R* between the synthetic seismograms and the real data is given by the following equation:

$$R = \frac{(\mathbf{u} - \mathbf{G}\mathbf{m})^{\mathrm{T}}\mathbf{W}(\mathbf{u} - \mathbf{G}\mathbf{m})}{\mathbf{u}^{\mathrm{T}}\mathbf{W}\mathbf{u}}. \tag{8}$$

For the numerical computation of the GFs, the same code (EFISPEC3D) as for the synthetic test (Section 4.2) was used. The GFs were calculated for a source position obtained with the semblance method (see Section 4.3) for the 5 best VLP events (highest signal-to-noise ratio; events 7, 11, 17, 18 and 23 in Table 3), which are clustered within a few hundred m. Like for the semblance method, here we use a homogeneous model (V_P = 2.2 km/s, V_S = 1.272 km/s and ρ = 2120 kg/m^3) for the computations of the Green's functions. As discussed above, the

use of a homogeneous model is justified due to the large VLP wavelengths compared to the dimensions of the experiment.

Seismograms on volcanoes are often recorded in the near-field of seismic sources, where tilts can form a considerable part of the seismic ground motion. Such tilts can have a first-order effect on horizontal seismograms at long periods (e.g. Rodgers, 1968; Graizer, 2005). Maeda et al. (2011) proposed a new method of including tilt into seismic inversions by including it into the GFs. Van Driel et al. (2015) improved and simplified this approach by including the computation of rotational motion directly in a high-order finite elements method. Here we use their method to create sets of GFs with and without tilts incorporated in the horizontal components.

In EFISPEC, the rotations are directly obtained from the derivatives of the numerical solution in the code, rather than approximated with a central differences method at mini-arrays around the station (as in Van Driel et al., 2015). The gravitational acceleration affecting the horizontal components are expressed using the spatial derivatives of the ground motion:

$$a_i = \frac{1}{2}\left(\frac{\partial u_3}{\partial x_i} - \frac{\partial u_i}{\partial x_3}\right) \cdot g, \qquad i = 1,2 \tag{9}$$

with the gravitational constant g, and the displacements u_i, where $i = 1,2$ indicate the horizontal and $i = 3$ the vertical directions x_i. The tilt traces are numerically double integrated and added to the corresponding displacement GFs. As the tilts lead to offsets in the displacement GFs (as they represent acceleration pulses), the FFT based inversion can become unstable. We stabilise the result by (i) double differentiating the GFs and (ii) differentiating the velocity data, the same as in Van Driel et al. (2015).

We use 6 different datasets for the inversion: the five single events named above (events 7, 11, 17, 18 and 23) as well as the stack of all 25 VLP events. For the latter, the unfiltered waveforms of all events were aligned and stacked based on the cross-correlation in the frequency band 0.03 – 0.125 Hz, with a correlation coefficient threshold of 0.8. This resulted in a significant noise reduction, particularly on the horizontal components. In preparation for the inversion, the data is corrected for the instrument response, filtered between 0.04 and 0.125 Hz and integrated to displacement. It is important to mention that the alteration of the VLP displacement waveforms due to the filtering was very subtle, consistent with our attempt to minimise the alteration of waveforms prior to inversion. For the inversion, we use all the seismograms except the faulty east-west components at stations WI02 and WI04 (see above) and all data is weighted equally.

5.2 Inversion Results

We first analyse the results of the inversion for the stack. The obtained waveform fits are plotted in Fig 12, showing generally a good fit between synthetic and real data (R = 0.12). The horizontal components at the stations WIZ, WI14 and WI15 are not well reproduced. This is likely a consequence of a small error in the source location, which can have a strong influence on the waveforms at stations close to the source. However, as the large majority of seismograms fit very well, we consider the solution robust.

The resulting full-waveform moment tensor solutions are shown in Fig 13A. The diagonal moment tensor elements M_{xx}, M_{yy} and M_{zz} dominate the solution, while the off-diagonal elements are very small in comparison. The solution shows similar source-time history for all six moment-tensor components. We use the principal component analysis based on singular value decomposition (Vasco, 1989) to assess the similarity between the retrieved components

474 and to extract a unique source-time function representative for all the components. The
475 resulting singular values are shown in Fig 13B, confirming that a single STF is suitable to
476 describe the inversion results.

477 The resulting source time function (time-history of the source slip) for the stacked traces is
478 shown in Fig 13C. There is a striking similarity between the slip time-history and recorded
479 displacement, which confirms that the wavefield is dominated by the near- and intermediate-
480 field terms (which are directly proportional to the source movement; see Lokmer and Bean,
481 2010), while the propagation of the far-field *P* and *S* is negligible in comparison. Table 5
482 shows the corresponding moment-tensor components for both the stack and the results of the
483 single VLP events. For the single events, despite the varying amplitude, the relative
484 contributions of the different moment tensor components are very consistent between events,
485 supporting a repeating source mechanism. We proceed decomposing the stack solution next.
486 The inversion including tilts in the Green's functions will be addressed thereafter.

487

488 **5.2.1 Moment-tensor decomposition**

489 Following the decomposition method of Vavryčuk (2001), our moment-tensor solution
490 consists of 75% isotropic, 13% CLVD and 12% double-couple (DC) component. The ratio of
491 the principal values (PVs) of the stack solution is 1:1.2:1.8, where the eigenvector
492 corresponding to the largest principal value is quasi-horizontal and pointing approximately to
493 the North (**T** (E, N, UP) = [0.1 0.98 -0.14]). Moreover, 4 out of 5 individual events yield the
494 same ratio of principal values, while the remaining event has the ratio 1:1.2:1.9. Such a
495 robust result makes it possible to infer more detail about the source geometry: specifically,
496 we search for the best-fit solution assuming a crack with a mixed tensile-shear mode of
497 failure (Fig 14A), like in Dufumier and Rivera (1997) and Vavryčuk (2001). For $\alpha = 0$ º the

source is a pure DC, for $\alpha = 90^{o}$ it is a pure tensile crack, while for all other angles it is a combination of both. Assuming such a source geometry appears to be plausible because (i) the ratio of principal values suggests a quasi-tensile crack and (ii) a crack geometry is the most likely candidate for fluid transport inside a shallow volcanic plumbing system (Chouet, 2003).

According to Dufumier and Rivera (1997), the moment-tensor of such a source in the coordinate system of principal axis is written as:

$$\mathbf{M} = \mu AD \begin{bmatrix} \sin(\alpha)(K+1)-1 & 0 & 0 \\ 0 & K\sin(\alpha) & 0 \\ 0 & 0 & \sin(\alpha)(K+1)+1 \end{bmatrix}, \qquad (10)$$

where A is the area of the crack plane, D is the amount of slip, α is the inclination of the slip from the crack plane, and $K = \lambda/\mu$ is the ratio of Lamé constants (note that the principal values in Eq. (10) appear in ascending order). In order to compare the theoretical principal values, PV_t, from Eq. (10) with our diagonalized moment-tensor solution (PV), we normalize both sets of principal values with the largest ones and define the L2-misfit (R_2) as:

$$R_2 = \frac{(\mathbf{PV}_t - \mathbf{PV})(\mathbf{PV}_t - \mathbf{PV})^T}{\mathbf{PV} \cdot \mathbf{PV}^T} \cdot 100\% \ , \qquad (11)$$

where

$\mathbf{PV_t} = \left[PV_t(1)/PV_t(3) \quad PV_t(2)/PV_t(3) \right]$ and

$\mathbf{PV} = \left[PV(1)/PV(3) \quad PV(2)/PV(3) \right]$.

In order to minimize the R_2 misfit (Eq. (11)), we perform a grid search over the (α, K)–space, where α ranges from 0° to 90° and K ranges from 1 to 10.

Dufumier and Rivera (1997) and Vavryčuk (2001) point out that the parameter K is a property of the fault/crack and it should be inverted for rather than calculated directly from the velocities of seismic waves in the surrounding medium. The source region is a zone of weakness and can have significantly different rheological properties than the surrounding medium. Neglecting this fact may lead to an incorrect determination of the source parameters.

The result of our search for the minimum residual R_2 is shown in Fig 14B. The contours represent the misfit between the theoretical and observed principal values of the moment tensor. The absolute minimum is denoted by the blue solid circle and corresponds to K = 6.7 and slip angle $\alpha = 27^{o}$ (Fig 14A). Since the principal tension axis halves the angle between the slip direction and the crack normal, it turns out that the crack is dipping at 67^{o} northward like shown in Fig 15A. However, although our moment-tensor solution was very robust between 5 events and the stack, the uncertainties in the velocity model, source location and noise contaminating the data are likely extending possible source candidates to several percent of the misfit function. Thus, we also show a pure tensile solution, where $K = 3$ and $\alpha = 90^{o}$ (Fig 15B). Nevertheless, our solutions show that caution should be exercised when interpreting moment-tensor solutions for volcanic signals.

5.2.2 Volumetric change in VLP source

In the previous section, we pointed out the ambiguity in the inferred source mechanism and the elastic properties of the source region. Here we assess the volumetric change in the VLP source for both source candidates shown in Fig 15.

The isotropic moment ($\mathbf{M_0^{ISO}}$) of a general moment-tensor (**M)** is defined as:

$$\mathbf{M_0^{ISO}} = \frac{1}{3} tr(\mathbf{M}) \quad (12)$$

Combining Eqs. (10) and (12) yields:

$$\mathbf{M^{ISO}} = AD\sin(\alpha)(\lambda + \tfrac{2}{3}\mu), \quad (13)$$

where $AD\sin(\alpha)$ is equal to the volume change ΔV, which is illustrated in Fig. 14A. This gives the relationship between the isotropic moment and the volume change of the source with the crack-like geometry:

$$\mathbf{M^{ISO}} = \Delta V(\lambda + \tfrac{2}{3}\mu). \quad (14)$$

On the other hand, the moment tensor retrieved from the stacked signals (Table 5) is equal to:

$$\mathbf{M} = 1.6 \cdot 10^{12} \begin{bmatrix} 0.69 & 0.03 & -0.02 \\ \mathbf{0}.03 & 1 & -0.06 \\ -\mathbf{0}.02 & -0.06 & 0.58 \end{bmatrix} \mathrm{Nm}, \quad (15)$$

where the isotropic moment (Eq. (12)) is equal to $\mathbf{M_0^{ISO}} = 1.2 \cdot 10^{12}\,\mathrm{Nm}$.

In order to estimate the elastic parameters in the source region and the volume change of VLP sources, we use a P-wave velocity ($V_p = [(\lambda+2\mu)/\rho]^{1/2}$) ranging between 1.3 and 2.3 km/s (see Section 3), the density of 2160 kg/m^3 and the retrieved parameter $K = \lambda/\mu$ to estimate the elastic parameters of the source region and the volume change in VLP sources. The results for both cases presented in Fig 15 are given in Table 6.

The pure tensile and shear-tensile crack mechanisms yield a comparable volume change when the same P-wave velocity is assumed. However, the results corresponding to the velocities of 2.3 km/s and 1.3 km/s, respectively, give the lower and upper bounds (145 – 450 m^3) for the volume change, which encompass the solutions obtained for Stromboli volcano

559 (Chouet et al, 2003), Mt Etna (Zuccarello et al., 2009), Mt Erebus (Aster et al., 2008) and
560 dike volume change on Popocatepetl volcano (Chouet et al., 2005). However, these authors
561 dealt with the same ambiguity in the choice of the elastic properties of the medium.

562 **5.2.3 Inversion including tilt**

563 For the additional inversion, where tilt was included in the Green's functions, the moment
564 tensor solution (Table 5) is even more dominated by the isotropic component (86%) and only
565 small CLVD (4%) and DC (10%) components. Given the noise and uncertainties in the result,
566 we regard it a nearly isotropic source mechanism; more accurately, only a slightly anisotropic
567 with the horizontal N-S direction of maximum stress. However, the above decomposition
568 showed that a wide range of possible candidates is suitable to describe the same moment
569 tensor.

570 While the fit for the horizontal components at stations WI12, WI14 and WI15 is much better
571 than for the tilt-free case, the overall waveform fit is not as good as before (R = 0.31). The
572 uncertainties in the source location may provide a reason for this – a relatively small change
573 in depth can strongly change the amount of tilt in the GFs. Furthermore, large-scale strain can
574 be converted into local rotations (strain rotation coupling; Van Driel et al., 2012), an effect
575 not modelled in the GFs. If this coupling is consistent over several stations, it may bias the
576 obtained results (Van Driel et al., 2015).

577

578 **6. Discussion**

579

580 **6.1 Semblance and arrival time locations**

One goal of this work lies in determining if HF, LP and VLP source processes are from different spatial locations. In this context, we note that the genetic processes that produce the three event types may occur in different parts of the hydrothermal/magmatic system. The location of the three source excitations is also important in the context of our observation that the VLP source process precedes the LP and HF excitation (see examples in Fig. 3 and 4). Based on the given locations and uncertainties (Table 3 and Fig 11), we regard the HF, LP and VLP to have systematically different source positions and wish to examine their significance in the context of the location procedures and associated uncertainties.

We first note that HF source locations appear to be systematically shallower (<1 km) than the earlier VLP sources (~1 km depth). The VLP sources have highly similar waveforms, which may be regarded as evidence for a repeating source process and strong rectilinearity that is expressed in the semblance values.

In contrast, the LP sources have very low semblance values which are probably due to a significant departure in rectilinearity for these events. Indeed, some of the LP events have unbounded location uncertainties (having error bounds larger than the search grid) (Table 3 and Fig 11 shallow events), suggesting that their locations should be treated with great caution.

In the context of our synthetic results, we regard semblance location uncertainties as due to several effects including: 1) the elevated noise levels within the LP and VLP signals, 2) variations in local velocity structure and their departure from the average values found using active source and ambient noise data, 3) departures from the isotropic source processes, and 4) near-field effect (e.g., see Lokmer and Bean, 2010). The effects of noise are shown directly in our synthetic analysis (Table 4, compare synthetics case 1 with 3 and case 6 with 8) where the semblance is shown to decrease with increased noise. This effect is also seen by

605 comparison of the signal-to-noise ratios and the computed semblance (see Table 4 and Fig
606 10). It is clear that the coherence of isotropic components may be significantly contaminated
607 by noise sources especially for SNR values below 3, so the interpretation of the signals where
608 SNR < 3 should not be attempted.

609 In addition, the semblance values show that some source geometries (e.g., high angle tensile
610 cracks) may produce significant departures in radial coherence (and lower semblance values).
611 We suggest here that such cases may be diagnosed if recorded on dense array networks where
612 discrepancies will tend to reduce the coherence as seen in the semblance computation.

613 The synthetic results suggest, however that azimuthally symmetrical sources (such as a
614 horizontal tensile crack or a vertical pipe) may generally be indistinguishable from isotropic
615 sources (compare Table 4 synthetics case 1, 4) from a semblance computation approach. Our
616 results suggest that a horizontally layered structure may also yield systematic mis-locations in
617 the data (compare Table 4 synthetic case 1, 7), but note in our case that the velocity structure
618 is probably better constrained than some other volcanic systems (Section 3). We also note,
619 based on our synthetic analysis, that vertically oriented dykes will tend to have poorly
620 retrieved locations, low semblance values and large location errors (Table 4, Case 6 and 8).

621 In this context, we note that VLP sources are generally located at the southern margin of the
622 Crater and at 1 km depth. This position is roughly coincident with the southern margin
623 fumaroles (Fumarole 0 and Fumarole 1 in Fig 1), which are thought to tap into gases having
624 strong magmatic signatures . In addition, the deformation signatures from long term levelling
625 surveys (Peltier et al., 2009; Fournier and Chardot, 2012) suggest that deformation within the
626 crater tephra fill is centred at very shallow depth (a few hundred m below the surface), on the
627 margin of the southern crater wall. Both studies showed that the range of magmatic and
628 hydrothermal deformation over the past several decades could be explained by the flux of

629 fluids and heat into the shallow hydrothermal system. Interestingly, our HF sources are
630 located beneath the central crater lake and not the southern margin, which might be viewed as
631 discrepant with the shallow deformation results. Christenson et al. (submitted), noted that
632 lake level changes match closely to periods of shallow deformation. Given the modestly
633 higher velocities for the Rayleigh wave interferometry (2.2 km/s vs 2.4 km/s) yield modestly
634 shallower locations having the same epicentre cluster, we regard the HF locations as mostly
635 within the shallow volcano hydrothermal system, possibly caused by repeated failure of
636 critically stressed rocks in the conduit environment. The results are consistent however with
637 locations obtained by Nishi et al. (1996) from a short-period array deployment to White
638 Island. In that study, high frequency earthquakes, referred to as spasmodic and volcano-
639 tectonic earthquakes, were distributed mostly at very shallow depth beneath the central crater
640 and present day crater lake. The spectral content for the earlier earthquakes is significantly
641 higher, peaked at 5-10 Hz, than those observed by our broad-band deployment (peaked at 2-5
642 Hz) and may have a different genetic provenance. Given the flat response characteristics of
643 both short-period and broadband seismometers in the common frequency band, we regard the
644 source process for our HF earthquakes as different from those identified by Nishi et al.
645 (1996).

646 **6.2. Source inversion**

647 We obtained a robust solution for the VLP source inversion, where the most likely source
648 mechanism is a quasi-vertical, steeply North-dipping tensile crack with a significant amount
649 of shear movement in the dipping direction. It was pointed out that the elastic constants of the
650 source region should not be mixed with those from the surrounding medium, as it can result
651 in retrieving incorrect source parameters. In the case of LP events, we cannot robustly invert
652 for detail of the source mechanism, so we often *a priori* constrain the solution (e.g., Nakano
653 and Kumagai, 2005; Lokmer et al., 2007; De Barros et al., 2011), and we suggest that caution

654 be exercised when decomposing the solutions of VLP inversions. When tilt was included in
655 the computed GFs, the results pointed towards a more isotropic source mechanism.

656 The volume change is estimated to be 145 m^3 – 450 m^3, which is in agreement with the
657 results reported at different volcanoes (see references in the last paragraph of Section 5.2.2).
658 In all these examples, the VLP pulses are attributed to the ascent of a gas slug. Interestingly,
659 Zuccarello et al. (2009) estimated that the cumulative volume change of VLP sources
660 contributed to only about 5% of the total gas emission on Mt. Etna volcano, a result that
661 points to uncertainties in the mass balance between gas transmission at depth and subsequent
662 discharge at the surface. However, the reason might be more trivial: if there are significantly
663 lower frequencies present in the recorded VLP signals, we would not be able to recover them
664 truthfully due to the band-limited nature of our instruments. If this is the case, then the
665 retrieved source-time function (Fig 13C) does not represent the true time-history of the slip in
666 the source, but it is rather its filtered representation, and may have significantly lower
667 amplitude than the true process. This scenario is very likely for slow processes of small
668 magnitude, whose duration is comparable to or longer than the lower frequency limit of the
669 recording instrument. Maeda et al (2015a, b) recognized this problem and performed a search
670 for the parameters of elementary functions (ramp, Gaussian pulse and triangle, see Fig 7 in
671 Maeda et al., 2015a) whose filtered version corresponded well to the retrieved source-time
672 function. Here we suggest that such a possibility should not be ignored and caution should be
673 exercised when directly linking the retrieved source function to a source process.

674

675 **6.3 Interpretation of White Island fluid flux from coupled earthquakes**

676 We next examine the process that might generate the three coupled event types based on their
677 timing and location. We noted earlier that the main VLP event onset precedes the HF and LP

678 sources by a few seconds. The HF and LP sources arrival times are difficult to distinguish in
679 our case, but we do note that the LP source extends in time beyond the coda for the HF event
680 type. In addition, the VLP is deeper (~1 km) than both the HF and LP sources. We do not
681 have strong confidence in the LP source locations (Fig 11), due to the strong departures from
682 radial particle motions (see synthetics section 4.2), but propose that the HF source process is
683 associated with very shallow portion of the crater system.

684 We place the event types in the context of an existing conceptual model for the White Island
685 volcanic system (Fig 16), composed of a shallow magma storage region overlain by a shallow
686 convecting hydrothermal system (e.g., Christenson and Wood, 1993; Werner et al, 2008).
687 The hydrothermal system likely includes strong permeability contrasts from inherent rock
688 porosity and the fragmental vent system, which is cut by fumarolic pathways to the surface
689 and into the crater lake. The hydrothermal system includes a single phase vapour within the
690 high flux pathways and near the magma interface. Away from the fumarolic pathways and at
691 shallower depth, the single phase gas is replaced by a two phase system including fluids and
692 gas, which in turn gives way to a single phase fluid at the crater lake near surface water table.
693 Convection and persistent degassing is driven by heat and gas from the shallow magma
694 system (Fig 16).

695 We propose the VLP source process as possibly caused by the release of gas and fluids that
696 have ponded behind the top of the magma conduit (Fig 16). The ponding may be akin to a
697 bubble trap (e.g., Adelstein et al, 2015) owing to a mostly impermeable magma carapace (Fig
698 16), which has been inferred at White Island (Cole et al 1999) based on geophysical
699 constraints from eruptive activity in 1977 (Clark and Otway, 1989; Houghton and Nairn,
700 1989). Release of slowly pressurized fluids from the bubble trap may cause upward
701 migration and very long period collapse and recovery behind the trap. It is uncertain if this
702 pressurisation step is linked to the observed 30 second onset of the VLP signal, shown in the

low noise examples in Fig 4, which in our case may be the slow deformation onset seen in their Fig 2 (Maeda et al., 2015b). In this case, the primary VLP oscillation (rupture onset) may be observed as a strongly isotropic radiation pattern, consistent with rupture of the carapace. The rupture would include both tensile and shear crack components (Fig 15) as the carapace fails. Hot ductile conditions near the magma would promote rapid healing of the carapace after the VLP and the introduction of new gas would quickly re-pressurise the top of the magma system. The time frame of rupture and healing in this case may be on the order of the inter-event times for the coupled earthquakes (about 2 to 3 hours). The moment tensor inversion and volume computation are computed assuming elastic conditions in the source medium. It is uncertain if such conditions would be satisfied for the seismological time frames seen for VLP at White Island. At Kilauea volcano, Hawaii, zones of hot weak rock (Dawson et al., 1999) are interpreted from strong V_p/V_s contrasts (and attendant high Poisson ratios) found from travel-time tomography. Ohminato et al, (1998) suggests that high Poisson ratios (~0.33) may be required to explain moment tensor solutions for tensile crack excitations inferred at that volcano. At White Island, the inferred magma carapace would have similar rock mechanical conditions and could be the locus of VLP source processes. We note however, that our moment tensor inversion (Section 5.2.2) does not provide information about the elastic rock conditions at the source. Instead, these may be viewed as inversion parameters for discontinuities (e.g., faults). This is highlighted in Dufumier and Rivera (1997) and Vavrycuk (2001). In fact, Vavrycuk (2001) used the Poisson ratio as a parameter to separate realistic and unrealistic source mechanism solutions. If we accept that the VLP represents a fault-like rupture of the magmatic carapace, then the rupture process may be elastic for time frames similar to the VLP and ductile for longer timeframes (Melosh, 1980).

727 Meanwhile, as the gas slug proceeds to shallower depth, the onset of LP and HF excitations
728 begin. We emphasise that the short time delay between the primary VLP and LP/HF source
729 onsets may preclude gas slug migration as a viable mechanism for the shallow seismicity.
730 Gas slug migrations times (James et al., 2006) for gas through fluids are probably an order of
731 magnitude too slow to account for the excitation of source positions as much as 500 m apart.
732 If instead the gas pulse is propagating through a single phase gas (e.g. Christenson et al,
733 2010), then the propagation times might be faster. For the former, the fluid/gas pressure
734 above the ascending gas slug may act to perturb critically stressed portions of the shallow
735 hydrothermal system leading to HF (Nishi et al, 1996) and LP activity (e.g., Chouet, 1993;
736 Neuberg et al, 2000) in the shallow hydrothermal system. For the latter, the rapid propagation
737 of the gas slug may directly induce the HF seismicity as discussed below. We note that
738 significant overpressures/underpressures may be achieved from the passage of gas slugs
739 through conduit flares (James et al, 2006). In our case, LP and HF activity may not be a
740 direct result of the gas slug propagating through a flared conduit. Instead, we surmise that the
741 locus of shallow seismicity may be focused at points of stress concentration and may include
742 flares or constrictions within the hydrothermal conduit system. Similarly, the HF and LP
743 events are not interpreted as an example of the hybrid event type first described by Lahr et al.
744 (1994) due to the variable timing between HF and LP sources . This may be illustrated by
745 stacking coherent LP waveforms for a given event (example completed using event 11 in Fig
746 3 and Table 1) and then noting small migrations (a few tenths of a second) in the onset of the
747 HF component (Fig 17). The LP-HF timing offset might occur either by the variable
748 propagation speeds of HF body waves and LP surface waves to the dense array of stations, or
749 may alternatively imply a different physical location for the two wave types. The small
750 timing offsets suggest the later in our case. In addition, we note that the LP source process,
751 while coherent station-to-station (Fig 17A) are not strongly coherent from event-to-event (Fig

752 17C), based on an analysis of the waveform cross correlation. The lack of coherence can be
753 partially explained by the strong effects of noise on the LP source (compare Fig 17C to Fig
754 3), but significant variation in waveform coherence is seen for periods having low noise
755 levels (see variation in coherence for events 15-23 in Fig 17 C). By contrast. coherence for
756 VLP events is very high (Fig 17D) for all events of the sequence. This implies that the VLP
757 events are repetitious in nature while the LP component represents a more variable source
758 process. Results suggest that the LP source process seen here may be different from those
759 observed by Sherburn et al., (1998), based on the strong event similarity seen in the earlier
760 study.

761 We also consider the coupled event types in the context of the possible modes of material
762 failure at White Island. For example, Heap et al, (2015) noted that hydrothermally altered
763 lavas at White Island will favour dilatant failure to depths of 2 km while ash tuffs convert
764 from dilatational to compactant modes at depths of ~250 m. Further, Heap et al. (2015)
765 suggest that White Island ash tuffs, which are prone to low pressure failure from pore
766 collapse, may promote small, long rupture duration events such as LP seismicity (Bean et al.,
767 2014) at very shallow depths. However, it is difficult to envisage the repeating failure of
768 coupled LP and HF events for two separate rock types distributed within a few seconds of
769 each other and this may be implausible for these earthquakes. We regard the mechanical
770 failure modes outlined by Heap et al. (2015) as more appropriate for VT and LP type activity
771 found by Nishi et al., (1996) and Sherburn et al. (1998), which may have different genetic
772 source process than for the coupled events described here. In our case, we favour failure of
773 the magma carapace as the source for VLP, resonance associated with fluid migration as the
774 source for shallow LP activity and the rapid failure of critically stressed conduit materials as
775 the source for HF events. We note similarities between the observations in our study, and
776 those at Satsuma-Iwojima volcano in Japan (Ohminato, 2006) which documented VLP

coupled with LP burst activity. We note however that Ohminato (2006) suggested a very difference source process, linking the activity to the repeated excitation of boiling water to the very shallow hydrothermal system. This contrast in interpretation illustrates the need for detailed understanding of source location and process in the interpretation of seismic signals from volcanic systems.

7. Conclusions

We completed a detailed analysis of 25 coupled HF, LP and VLP earthquakes recorded on a dense array deployment at White Island between 19-21 August 2011. We find that the VLP component precedes the HF and LP components of the activity by a few seconds. The VLP signals have generally deeper locations (~1.0 km) than the HF and LP events (<1 km), based on locations using waveform semblance and arrival time earthquake locations.

The source processes producing the LP, VLP and HF source components are likely to be genetically linked to the rapid flux of fluids (gas and/or liquid phases) from the magma system into the shallow hydrothermal system. Moment tensor inversion of the VLP events, which are centred below two high gas discharge fumaroles, is consistent with a high angle north dipping and east-west striking tensile crack. Each tensile excitation includes a modest shear component directed down the dipping plane.

Each VLP event is interpreted as a repeating excitation of this stationary crack above a shallow magma storage region. We surmise that, at low excess pressures, the crack releases gasses passively, but for strong gas flux periods, the gas release produced discrete VLP-HF and LP source excitations. The volume change associated with the VLP component is about

145-450 m^3 while the moment release is ~$1.2x10^{12}$ Nm. Each event may therefore reflect the release of gas from the magmatic hot ductile carapace into the overlying hydrothermal system. The HF and LP components may represent the seismic response of fluids pressurisation in the overlying hydrothermal system. The LP source may either be associated with resonant fluid migration (e.g., Chouet, 1996; Neuberg et al, 2002), or less likely, the failure of low tensile strength ash tuff materials (Heap et al., 2015; Bean et al., 2014). The HF earthquakes may result from either brittle failure of higher strength lava flow materials (Heap et al., 2015), or more likely the rapid failure of critically stressed rock in the hydrothermal conduit. Gas slug ascent rates within a fluid filled conduit are probably too slow (James et al., 2006) to produce LP/HF seismicity at shallow depth in our case but slug ascent within a pre-existing single phase gas column may promote more rapid gas ascent. In the former case, the shallower seismicity is possibly due to either stress transmission directly through the rock or via fluid pressure transfer in the hydrothermal conduit system. In the latter case, gas ascent itself may initiate HF and LP activity. Future work will examine additional occurrences of VLP activity specifically associated with eruptive activity in October 2013.

Acknowledgements

This research was funded by the Ministry of Business, Innovation and Employment (MBIE) to GNS CORE funded research (AJ, JS and BF) and the Earthquake Commission (EQC) (AJ, IL). JT received funding from the European Union's Seventh Framework Programme under Grant No. 289976 (Project NEMOH). The dense array deployment was completed by Steve Sherburn, Craig Miller, Tony Hurst, Richard Johnson, Nico Fournier, Brad Scott and (AJ). Xiaoming Wang is thanked for providing the bathymetry data used in this study. Florent De

824 Martin is thanked for his assistance with the EFISPEC3D code. Useful comments by Bruce
825 Christenson and John Ristau improved an early version of the manuscript and early
826 discussions with Nico Fournier supported early stages of this work. Fig 16 was developed
827 from earlier conceptual models first derived by Bruce Christenson.

828

829 **References:**

830 Almendros, J., Chouet, B., Dawson, P., Bond, T., 2002. Identifying elements of the plumbing
831 system beneath Kilauea Volcano, Hawaii, from the source locations of very-long-period
832 signals. Geophys. J. Int. 148, 303–312.
833
834 Almendros, J. & Chouet, B., 2003. Performance of the radial semblance method for the
835 location of very long period volcanic signals. Bull. Seis. Soc. Amer. 93 (5), pp. 1890-
836 1903.
837
838 Aster, R., Zandomeneghi, D., Mah, S., McNamara, S., Henderson, D., Knox, H., Jones, K.,
839 2008. Moment tensor inversion of very long period seismic signals from Strombolian
840 eruptions of Erebus Volcano. J. Volcanol. Geotherm. Res. 177, 635–647.
841
842 Bean, C., Lokmer, I., O'Brien, G., 2008. Influence of near-surface volcanic structure on long-
843 period seismic signals and on moment tensor inversions: Simulated examples from Mount
844 Etna. J. Geophys. Res. 113, B08308. doi:10.1029/2007JB005468.
845
846 Bean, C.J., De Barros, L., Lokmer, I., Métaxian, J.-P., O'Brien, G.S., Murphy, S., 2014.
847 Long-period seismicity in the shallow volcanic edifice formed from slow-rupture
848 earthquakes. Nat. Geosci. 7, 71–75.
849
850 Burton, M.R., Oppenheimer, O., Horrocks, L.A., Francis, P.W., 2000. Remote Sensing of
851 CO2 and H2O emission rates from Massaya volcano, Nicaragua. Geology 28,10,915-918.
852
853 Chardot, L.; Jolly, A.D.; Kennedy, B.; Fournier, N.; Sherburn, S., 2015. Using volcanic
854 tremor for eruption forecasting at White Island volcano (Whakaari), New Zealand. J.
855 Volcanol. Geotherm. Res. 302*:* 11-23. doi: 10.1016/j.jvolgeores.2015.06.001.
856
857 Christenson, B.W., Wood, C.P., 1993. Evolution of a vent-hosted hydrothermal system
858 beneath Ruapehu Crater Lake, New Zealand. Bull. Volcanol. 55: 547-565.
859
860 Christenson, B.W.; Reyes, A.G.; Young, R.; Moebis, A.; Sherburn S.; Cole-Baker, J.R.;
861 Britten, K., 2010**.** Cyclic processes and factors leading to phreatic eruption events :
862 insights from the 25 September 2007 eruption through Ruapehu Crater Lake, New
863 Zealand. J. Volcanol. Geotherm. Res. 191(1/2): 15-32.
864 doi:10.1016/j.jvolgeores.2010.01.008.
865

Chouet, B.A., 1996. Long-period volcano seismicity: its source and use in eruption forecasting. Nature 380, 309–316.

Chouet, B., 2003. Volcano Seismology, Pure App. Geophys. 160 (3-4), 739-788.

Chouet, B., Dawson, P., 2011. Shallow conduit system at Kilauea Volcano, Hawaii, revealed by seismic signals associated with degassing bursts. J. Geophys. Res. 116, p. B12317. doi:10.1029/2011JB008677.

Chouet, B., Dawson, P., Ohminato, T., Martini, M., Saccorotti, G., Giudicepietro, F., De Luca, G., Milana, G., Scarpa, R., 2003. Source mechanisms of explosions at Stromboli Volcano, Italy, determined from moment-tensor inversions of very-long-period data, J. Geophys. Res. 108 (B1), p. 2019. doi: 10.1029/2002JB001919.

Chouet, B., Dawson, P., Arciniega-Ceballos, A., 2005. Source mechanism of Vulcanian degassing at Popocatepetl Volcano, Mexico, determined from waveform inversions of very long period signals, J. Geophys. Res. 110, p. B07301, doi:10.1029/2004JB003524.

Clark, R. H., Otway, P. M., 1989. Deformation monitoring associated with the 1976–82 White Island eruptive sequence. In: Houghton, B. F. & Nairn, I. A. (eds) The 1976–82 Eruption Sequence at White Island Volcano (Whakaari), Bay of Plenty, New Zealand. New Zealand Geol. Surv. Bull. 103, 69–84.

Christenson, B.W., White, S., Britten, K., Scott, B.J., submitted. Hydrological evolution and chemical structure of a hyper-acidic spring-lake system on White Island, NZ, J. Volcanol. Geotherm. Res.

Cole, J.W., Thordarson, T., Burt, R.M., 2000. Magma Origin and Evolution of White Island (Whakaari) Volcano, Bay of Plenty, New Zealand, J. Peterol. 41, 6, 867-895.

Dawson, P.B., Chouet, B.A., Okubo, P.G., Villasenor, A., Benz., H.M., 1999. Three-dimensional velocity structure of the Kilauea caldera, Hawaii. Geophys. Res. Letts. 26 (18), 2805-2808.

Dawson, P.B., Chouet, B.A., Power, J., 2011. Determining the seismic source mechanism and location for an explosive eruption with limited observational data: Augustine Volcano, Alaska, Geophys. Res. Lett., 38, p. L03302. doi:10.1029/2010GL045977.

De Barros, L., Lokmer, I., Bean, C.J., O'Brien, G.S., Saccorotti, G., Métaxian, J-P., Zuccarello, L., Patanè, D., 2011. Source mechanism of long-period events recorded by a high-density seismic network during the 2008 eruption on Mount Etna, J. Geophys. Res. 116, B01304. doi:10.1029/2010JB007629.

De Martin, F., 2011. Verification of a Spectral-Element Method Code for the Southern California Earthquake Center LOH.3 Viscoelastic Case. Bull. Seis. Soc. Amer., 101(6), 2855–2865. doi:10.1785/0120100305.

Dufumier, H., Rivera, L., 1997. On the resolution of the isotropic component in moment tensor inversion. J. Geophys. Int. 131, 595-606.

Fournier, N., Chardot, L., 2012. Understanding volcano hydrothermal unrest from geodetic observations: insights from numerical modeling and application to White Island volcano, New Zealand. J. Geophys. Res. 117 (B11), B11208.

Francis, P., Burton, M.R., Oppenheimer, C., 1998. Remote measurements of volcanic gas compositions by solar occultation spectroscopy, Nature 396,6711, 567-570.

Fry, B., Deschamps, F., Kissling, E., Stehly, L., Giardini, D., 2010. Layered azimuthal anisotropy of Rayleigh wave phase velocities in the European Alpine lithosphere inferred from ambient noise. Earth Planet Sci. Letts. 297(1/2): 95-102 doi: 10.1016/j.epsl.2010.06.008.

Graizer, V. M., 2005. Effect of tilt on strong motion data processing. Soil Dyn. Earth. Eng., 25(3), 197–204. doi:10.1016/j.soildyn.2004.10.008.

Haney, M.M, Chouet, B.A., Dawson, P.B., Power, J.A., 2012. Source characterization for an explosion during the 2009 eruption of Redoubt Volcano from very-long-period seismic waves. J. Volcanol. Geotherm. Res. 259, 77-88. doi:10.1016/j.jvolgeores.2012.04.018.

Heap, M.J., Kennedy, B.M., Pernin, N., Jacquemard, L., Baud, P., Farquharson, J.I., Scheu, B., Lavallee, Y., Gilg, H.A., Letham-Brake, M., Mayer, K., Jolly, A.D., Reuschle, T., Dingwell, D.B., 2015. Mechanical behaviour and failure modes in the Whakaari (White Island volcano) hydrothermal system, New Zealand. J. Volcanol. Geotherm. Res. 295: 26-42. doi:10.1016/j.jvolgeores.2015.02.012.

Hidayat, D., Chouet, B.,Voight, B., Dawson, P., Ratdomopurbo, A., 2002. Source mechanism of very-long-period signals accompanying dome growth activity at Merapi volcano, Indonesia. Geophys. Res. Lett., 29,2118–2121. doi:10.1029/2002GL015013.

Houghton, B.F., Nairn, I.A., 1991. The 1976–1982 Strombolian and phreatomagmatic eruptions of White Island, New Zealand: eruptive and depositional mechanisms at a ‘wet’ volcano. Bull. Volcanol. 54, 25–49.

Ingham, M.R., Bibby, H.M., Heise,W., Jones, K.A., Cairns, P., Dravitzki, S., Bennie, S.L., Caldwell, T.G., Ogawa, Y., 2009. A magnetotelluric study of Mount Ruapehu volcano New Zealand, Geophys. J. Int. doi:10.1111/j.1365-246X.2009.04317.x.

James, M. R., Lane, S. J., & Chouet, B. A., 2006. Gas slug ascent through changes in conduit diameter: Laboratory insights into a volcano-seismic source process in low-viscosity magmas. J. Geophys. Res.: Solid Earth. 1978–2012, 111(B5).

Jolly, A.D., Chardot, L., Neuberg, J., Fournier, N., Scott, B.J., Sherburn, S., 2012. High impact mass drops from helicopter: a new active source method, applied in an active volcanic setting. Geophys. Res. Lett. 39, L12306. http://dx.doi.org/10.1029/2012GL051880.

Kawakatsu, H., Ohminato, T., Ito, H., Kuwahara, Y., 1992. Broadband seismic observation at the Sakurajima volcano, Japan. Geophys. Res. Lett. 19 (19), 1959–1962.

Kawakatsu, H., Kaneshima, S., Matsubayashi, H., Ohminato, T., Sudo, Y., Tsutsui, T., Uhira, K., Yamasato, H., Ito, H., Legrand, D., 2000. Aso94: Aso seismic observation with broadband instruments. J. Volcanol. Geotherm. Res. 101, 129–154.

Kazahaya, K., Shinohara, H., Saito, G.,1994. Excessive degassing of Izu-Oshima volcano: magma convection in a conduit. Bull. Volcanol., 56, 207–216.

Kilgour, G., Manville, V., Della Pasqua, F., Graettinger, A., Hodgson, K.A, Jolly, G.E., 2010. The 25 September 2007 eruption of Mount Ruapehu, New Zealand: Directed ballistics, surtseyan jets, and ice-slurry lahars. J. Volcanol. Geotherm. Res. 191, 1–14.

Kilgour, G.N.; Blundy, J.; Cashman, K.; Mader, H.M., 2013. Small volume andesite magmas and melt-mush interactions at Ruapehu, New Zealand: evidence from melt inclusions. Contrib. Mineral. Pet. 166(2): 371-392. doi: 10.1007/s00410-013-0880-7.

Kumagai, H., Miyakawa, H., Negishi, H., Inoue, H., Obara, K., Suetsugu, D., 2003. Magmatic dike resonances inferred from very-long-period seismic signals. Science 299, 2058–2061.

Lahr, J. C., Chouet, B.A., Stephens, C.D. Power, J.A., Page, R.A., 1994. Earthquake classification, location, and error analysis in a volcanic environment: implications for the magmatic system of the 1989–1990 eruptions at Redoubt Volcano, Alaska. J. Volcanol. Geotherm. Res. 62, 137– 151.

Lee, W. H. K., Bennett, R. E., and Meagher, L., 1972. A method for estimating magnitude of local earthquakes from signal duration. Open file report, USGS.

Legas, A., Vandemeulebrouck, J., Revil, A., Kenma, A., Hurst, T., Reeves, R., Papasin, R., 2009. A case study of resistivity and self-potential signatures of hydrothermal instabilities, Inferno Crater Lake, Waimangu, New Zealand, Geophys. Res. Lett., 36, 12, L12306.

Lube, G., Breard, E.C.P., Cronin, S.J., Procter, J.N., Brenna, M., Moebis, A., Pardo, N., Stewart, R.B., Jolly, A. Fournier, N., 2014. Dynamics of surges generated by hydrothermal blasts during the 6 August 2012 Te Maari eruption, Mt. Tongariro, New Zealand. J. Volcanol. Geotherm. Res. 286, 248-262.

Lokmer, I., Bean, C., 2010. Properties of the near-field term and its effect on polarisation analysis and source locations of long-period (LP) and very-long-period (VLP) seismic events at volcanoes. J. Volcanol. Geotherm. Res. 192, 35-47.

Lokmer, I., Bean, C.J., Saccorotti, G., Patanè, D., 2007. Moment-tensor inversion of LP events recorded on Etna in 2004 using constraints obtained from wave simulation tests. Geophys. Res. Lett. 34, L22316, doi:10.1029/2007GL031902.

Maeda, Y., Takeo, M., 2011. Very-long-period pulses at Asama volcano, central Japan, inferred from dense seismic observations. Geophys. J. Int. 185(1), 265-282.

Maeda, Y., Takeo, M., & Ohminato, T., 2011. A waveform inversion including tilt: Method and simple tests. Geophys. J. Int. 184(2), 907–918. doi:10.1111/j.1365-246X.2010.04892.x.

Maeda, Y., Kumagai, H., Lascon, R. Jr., Figureoa, M.S., Yamashina, T., Ohkura, T., Baloloy, A.V., 2015a. A phreatic explosion model inferred from a very long period seismic event at Mayon Volcano, Philippines. J. Geophys. Res. 120(1), 226-242. doi:10.1002/2014JB011440.

Maeda, Y., Kato, A., Terakawa, T., Yamanaka, Y., Horikawa, S., Matsuhiro, K., Okuda, T., 2015b. Source mechanism of a VLP event immediately before the 2014 eruption of Mt. Ontake, Japan. Earth, Planets Space. 67:187, doi:10.1186/s40623-015-0358-0.

Menke, W., 1984. Geophysical Data Analysis: Discrete Inverse Theory (1st ed.). Orlando, USA, Academic Press.

Melosh, H.J., 1980, Rheology of the Earth: Theory and Observation, *in* Proceedings of the International school of physics "Enrico Fermi" Course LXXVIII, Physics of the Earth's Interior, *eds.* A.M Dziewonsky and E. Boschi, North-Holland Publishing Company, p. 318-336.

Molina, I., Kumagai, H., Garcia-Aristizabal, A., Nakano, M., Mothes, P., 2008. Source process of very-long-period events accompanying long-period signals at Cotopaxi volcano, Ecuador. J. Volcanol. Geotherm. Res. 176, 119–133. doi:10.1016/j.jvolgeores.2007.07.019.

Nakano, M., Kumagai, H., 2005. Waveform inversion of volcano seismic signals assuming possible source geometries. Geophys. Res. Lett. 32, L12302. doi:10.1029/2005GL022666.

Neidel, N., Tarner, M.T., 1971. Semblance and other coherency measure for multichannel data. Geophys. 36, 483–497.

Neuberg, J., Luckett, R., Ripepe, M., Braun, T., 1994. Highlights from a broadband array on Stromboli volcano. Geophys. Res. Lett. 21 (9), 749–752.

Neuberg, J., Pointer, T., 2000. Effects of volcano topography on seismic broad-band waveforms. Geophys. J. Int. 143, 239–248.

Neuberg, J., Luckett, R.. Baptie B., Olsen, K., 2000. Models of tremor and low-frequency earthquake swarms on Montserrat. J. Volcanol. Geotherm. Res.101, 83–104.

Nishi, Y., Sherburn, S., Scott, B.J., Sugihara, M., 1996. High-frequency earthquakes at White Island volcano, New Zealand: insights into the shallow structure of a volcano–hydrothermal system. J. Volcanol. Geotherm. Res. 72 (3–4), 183–197.

Nishimura, T., Nakamichi, H., Tanaka, S., Sato, M., Kobayashi, T., Ueki, S., Hamaguchi, H., Ohtake, M., Sato, H., 2000. Source process of very long period seismic events associated with the 1998 activity of Iwate Volcano, northeastern Japan. J. Geophys. Res. 105, 19,135–19,147.

Ohminato, T., 2006. Characteristics and source modeling of broadband seismic signals associated with the hydrothermal system at Satsuma-Iwojima volcano, Japan. J. Volcanol. Geotherm. Res. 158, 467–490. doi:10.1016/j.jvolgeores.2006.08.004.

Ohminato, T., Chouet, B.A., Dawson, P.B., Kedar, S., 1998. Waveform inversion of very-long-period impulsive signals associated with magmatic injection beneath Kilauea Volcano, Hawaii. J. Geophys. Res. 103, 23,839–23,862.

Park, I., Kim, K.Y., 2014. Shear Wave Velocity Structure Beneath White Island Volcano, New Zealand, from Receiver Function Inversion and H-κ Stacking Methods, Korean Soc. Earth Exp. Geophys., 17, 2, 66-73. http://dx.doi.org/10.7582/GGE.2014.17.2.066.

Peltier, A., Scott, B.J., Hurst, T., 2009. Ground deformation patterns at White Island volcano (New Zealand) between 1967 and 2008 deduced from levelling data. J. Volcanol. Geotherm. Res., 181, 207–218.

Prasetya, G. and Wang, X., 2011. Tsunami inundation modelling for Tauranga and Mount Maunganui. GNS Science Consultancy Report 2011/193. 36 p.

Rodgers, P. W., 1968. The Response of the Horizontal Pendulum Seismometer to Rayleigh and Love Waves, Tilts and Free Oscillations of the Earth. Bull. Seis. Soc. Amer., 58(5) 1384-1406.

Saccorotti, G., Lokmer, I., Bean, C.J., Di Grazia, G., Patanè, D., 2007. Analysis of sustained long-period activity at Etna volcano, Italy. J. Volcanol. Geotherm. Res. 160, 340–354.

Sherburn, S., Scott, B.J., Nishi, Y., Sugihara, M., 1998. Seismicity at White Island volcano, New Zealand: a revised classification and inferences about source mechanism. J. Volcanol. Geotherm. Res. 83 (3–4), 287–312.

Stehly, L., Fry, B., Campillo, M., Shapiro, N.M., Guilbert, J., Boschi, L., Giardini, D., 2009. Tomography of the Alpine region from observations of seismic ambient noise, Geophys. J. Int. 178(1) doi: 10.1111/j.1365-246X.2009.04132.x

Stevenson, D.S., Blake, S., 1998. Modelling the dynamics and thermodynamics of volcanic degassing. Bull. Volcanol. 60, 307–317.

Trovato, C., Lokmer, I., De Martin, F., Aochi, H., 2016. Long Period (LP) Events on Mt. Etna volcano (Italy): the influence of velocity structures on moment tensor inversion. J. Geophys. Int. doi: 10.1093/gji/ggw285.

Valentine, G.A., White, J.D.L., 2012. Revised conceptual model for maar diatremes: Subsurface processes, energetics, and eruptive products. Geol., 40, 12, 1111-1114.

Van Driel, M., Wassermann, J., Nader, M. F., Schuberth, B. S. a., Igel, H., 2012. Strain rotation coupling and its implications on the measurement of rotational ground motions. J. Seismol. 16(4), 657–668.

Van Driel, M., Wassermann, J., Pelties, C., Schiemenz, A., & Igel, H., 2015. Tilt effects on moment tensor inversion in the near field of active volcanoes. Geophys. J. Int. 202(3), 1711–1721. doi:10.1093/gji/ggv209.

Vasco, D. W., 1989. Deriving source-time functions using principal component analysis. Bull. Seis. Soc. Amer. 79(3), 711–730.

Vavryčuk, V., 2001. Inversion for parameters of tensile earthquakes. J. Geophys. Res. B: Solid Earth, 106(B8), 16339–16355. doi:10.1029/2001JB000372.

Wathelet, M., 2008. An improved neighborhood algorithm: parameter conditions and dynamic scaling. Geophys. Res. Lett., 35, L09301, doi:10.1029/2008GL033256.

Waite, G.P., Chouet, B.A. Dawson, P.B., 2008. Eruption dynamics at Mount St. Helens imaged from broadband seismic waveforms: Interaction of the shallow magmatic and hydrothermal systems. J. Geophys. Res. 113, B02305. doi:10.1029/2007JB005259.

Werner, C.A., Hurst, A.W., Scott, B.J., Sherburn, S., Christenson, B.W., Britten, K., Cole-Baker, J., Mullan, B., 2008. Variability of passive gas emissions, seismicity, and deformation during crater lake growth at White Island Volcano, New Zealand, 2002–2006. J. Geophys. Res. 113 (B1), 15.

Zuccarello, L., Burton, M.R.,Saccorotti, G., Bean, C.J., Patané, D., 2009. The coupling between very long period seismic events, volcanic tremor, and degassing rates at Mount Etna volcano. J. Geophys. Res.-Solid Earth 118 (9): 4910- 4921. doi: 10.1002/jgrb.50363.

Table 1: VLP filtered at 0.04-0.125 Hz. N is the event number and locations with error limits (in meters given in New Zealand Map Grid coordinates). Lateral and depth errors (er_l(z)) are in meters based on 2% error limit from the maximum semblance. SNR is the computed signal to noise ratio.

N	event easting	northing	depth	er_l(z)	semblance	SNR
1	2879980+/-170	6400000+/-130	880	660-1040	0.4774	2.3859
2	2879820+/-140	6400060+/-140	840	640-1000	0.5497	2.3355
3	2880020+/-150	6399840+/-130	940	740-1160	0.4909	1.9413
4	2880320+/-020	6400360+/-060	740	560-940	0.4730	2.7645
5	2880420+/-040	6400140+/-100	860	640-1060	0.4821	2.4670
6	2880100+/-130	6399880+/-140	920	720-1120	0.5278	2.3567
7	2880220+/-090	6400080+/-100	840	620-1000	0.6310	3.6471
8	2880000+/-110	6400100+/-130	900	700-1100	0.5720	2.8050
9	2880200+/-130	6400000+/-150	920	700-1100	0.5983	2.3324
10	2880360+/-030	6400100+/-090	820	640-1020	0.5263	2.9952
11	2880360+/-010	6400160+/-090	960	760-1180	0.5309	4.3236
12	2880060+/-160	6399800+/-120	920	720-1120	0.5180	2.8768
13	2880380+/-090	6400040+/-070	680	540-860	0.3955	1.5893
14	2880260+/-110	6400060+/-090	920	700-1100	0.6862	2.8702
15	2880360+/-020	6400080+/-090	960	720-1160	0.5961	3.4776
16	2879760+/-200	6399740+/-170	1120	880-1120	0.5654	2.4453
17	2880060+/-140	6399900+/-160	1040	820-1280	0.6724	4.5016
18	2880000+/-160	6399980+/-150	980	760-1180	0.6420	4.5097
19	2879800+/-140	6400020+/-130	1180	760-1180	0.4870	2.8766
20	2879980+/-190	6399820+/-150	1180	940-1440	0.5718	1.3369
21	2880000+/-180	6399940+/-140	960	740-1160	0.6191	3.2514

22	2880280+/-050	6400080+/-080	920	700-1100	0.6462	3.5423
23	2880240+/-070	6400080+/-090	960	740-1160	0.7133	4.3724
24	2880300+/-070	6400080+/-090	840	660-1040	0.5877	3.3617
25	2880020+/-140	6399920+/-090	520	400-640	0.1803	1.2227

Table 2: LP phase filtered 0.5-1.1 Hz. Error limits 50% of maximum semblance. See table 1.

N	event easting	northing	depth	er_l(z)	semblance	S/NR
1	2880160+/-240	6400400+/-190	280	20-920	0.1711	2.4994
2	2880200+/-190	6400440+/-110	300	60-620	0.0792	2.1020
3	2880300+/-110	6400500+/-070	320	160-460	0.0374	1.7694
4	2880220+/-290	6400480+/-160	400	60-1120	0.1751	2.2955
5	2880100+/---	6400300+/---	000	-----	-0.1121	1.2562
6	2880040+/---	6400220+/---	060	-----	-0.1245	1.3046
7	2880220+/-280	6400480+/-140	400	80-1180	0.1221	2.8868
8	2880180+/-240	6400444+/-140	260	140-240	0.1135	1.9039
9	2880320+/-290	6400440+/-190	440	60-1080	0.1631	2.7176
10	2880200+/-350	6400460+/-190	420	40-1400	0.2220	2.5738
11	2880340+/-190	6400400+/-120	300	100-600	0.0697	2.8215
12	2880260+/-360	6400480+/-200	560	100-1760	0.2255	4.0386
13	2880180+/-210	6400420+/-100	280	40-720	0.1036	2.0479
14	2880220+/-160	6400440+/-090	280	80-560	0.0689	2.4666
15	2880320+/-330	6400440+/-210	440	80-1340	0.2063	3.8058
16	2880160+/-310	6400420+/-180	420	20-1560	0.2535	6.5132
17	2880320+/-430	6400580+/-240	960	220-1980	0.1908	7.8226
18	2880280+/-310	6400480+/-170	500	100-1280	0.1570	4.2392
19	2880220+/-250	6400440+/-130	320	40-800	0.1289	2.5791
20	2880340+/-380	6400520+/-250	600	120-1840	0.2360	5.5220
21	2880180+/-290	6400420+/-240	280	20-1040	0.2150	2.9094
22	2880360+/-260	6400460+/-180	420	120-1260	0.1299	2.8239
23	2880180+/-270	6400420+/-190	280	00-780	0.1536	2.1955
24	2880120+/----	6400400+/----	180	-------	-0.0600	1.5858
25	2880000+/----	6400140+/----	20	-------	-0.1239	1.0630

Table 3: HF earthquake locations from hypo71 (Lee et al, 1972). Locations as described in Table 1, with lateral standard errors given by (seh) and depth standard errors given by (sez). The average root-mean-square (rms) has units of seconds.

	easting	northing	depth	seh(m)	sez(m)	rms
7	2880002	6400232	150	141	600	0.10
11	2880082	6400417	430	071	300	0.06
12	2880146	6400081	1350	212	1200	0.07
13	2880042	6400141	340	071	500	0.07
14	2880117	6400416	540	141	300	0.07
15	2880064	6400218	500	071	400	0.07
16	2880072	6400395	260	071	200	0.05
17	2880068	6400307	460	071	300	0.06

Table 4: Test of the waveform semblance location using a range of synthetic seismograms test cases. Eight cases examine the performance of the semblance method having the effects of variable source models, noise levels and noise levels. SynthN is the case number including the location (easting, northing and depth and description of the case. Synthetic seismograms are produced using the methods outlined in Section 4.2. The location recovered from the semblance analysis is computed using the methods outlined in Section 4.1.

Case				
synthN	event easting	northing	depth	description
sembN	event easting	northing	depth	semblance
Homogeneous model				
synth1	2880132	6400282	1000	explosive source
semb1	2880200	6400300	800	0.9733
synth2	2880132	6400282	2000	explosive source
semb2	2880200	6400200	1900	0.9568
synth3	2880132	6400282	1000	explosive source with noise
semb3	2880100	6400200	900	0.8473
synth4	2880132	6400282	1000	horiz. tensile crack

semb4	2880200	6400300	800	0.9762
Layered model				
synth5	2880132	6400282	1000	explosive source
semb5	2880200	6400300	600	0.9724
synth6	2880132	6400282	1000	oblique tensile crack#
semb6	2880600	6399500	2100	0.2652
synth7	2880132	6400282	1000	horiz. tensile crack
semb7	2880200	6400300	600	0.9749
synth8	2880132	6400282	1000	oblique tensile crack# w noise
semb8	2880600	6399600	900	-0.0032

oblique tensile crack oriented at strike 25° and dipping 75°.

Table 5: Results of the moment tensor inversion for the stack and 5 single events. The value A corresponds to the maximum moment tensor component, the other values denote the relative amplitudes of the individual moment tensor components M_{ij}. The last line shows the result for the inversion including tilt.

VLP Event	A (Nm)	M_{xx}	M_{yy}	M_{zz}	M_{xy}	M_{xz}	M_{yz}
Stack	1.60×10^{12}	0.69	1.00	0.58	0.03	-0.02	-0.06
7	2.13×10^{12}	0.63	1.00	0.55	0.05	-0.02	-0.06
11	1.96×10^{12}	0.67	1.00	0.56	0.03	-0.02	-0.06
17	2.11×10^{12}	0.66	1.00	0.56	0.04	-0.02	-0.06
18	1.83×10^{12}	0.68	1.00	0.57	0.04	-0.02	-0.06
23	1.98×10^{12}	0.67	1.00	0.56	0.04	-0.02	-0.06
Stack*	5.98×10^{11}	0.95	1.00	0.73	0.06	-0.03	0.02

Table 6: Parameters obtained for the VLP stack solution for a mixed shear-tensile crack mechanism as described by Dufumier & Rivera (1997) and Vavrycuk (2001). To calculate the volume change, the isotropic moment $M^{ISO}_0 = 1.2 \times 10^{12}$ Nm from the moment tensor inversion was used. To estimate elastic parameters and volume change of the source, we retrieved the parameter K by varying V_p at an assumed density of 2160kg/m^3 (see Fig 15).

v_p [km/s]	ρ [kg/m^3]	K	λ [GPa]	μ [GPa]	M_0^{ISO} [Nm]	ΔV [m^3]
1.3	2160	6.7	2.8	0.4	$1.2 \cdot 10^{12}$	391
2.3	2160	6.7	8.7	1.3	$1.2 \cdot 10^{12}$	125
1.3	2160	3	2.2	0.7	$1.2 \cdot 10^{12}$	450
2.3	2160	3	6.9	2.3	$1.2 \cdot 10^{12}$	142

Figure Captions

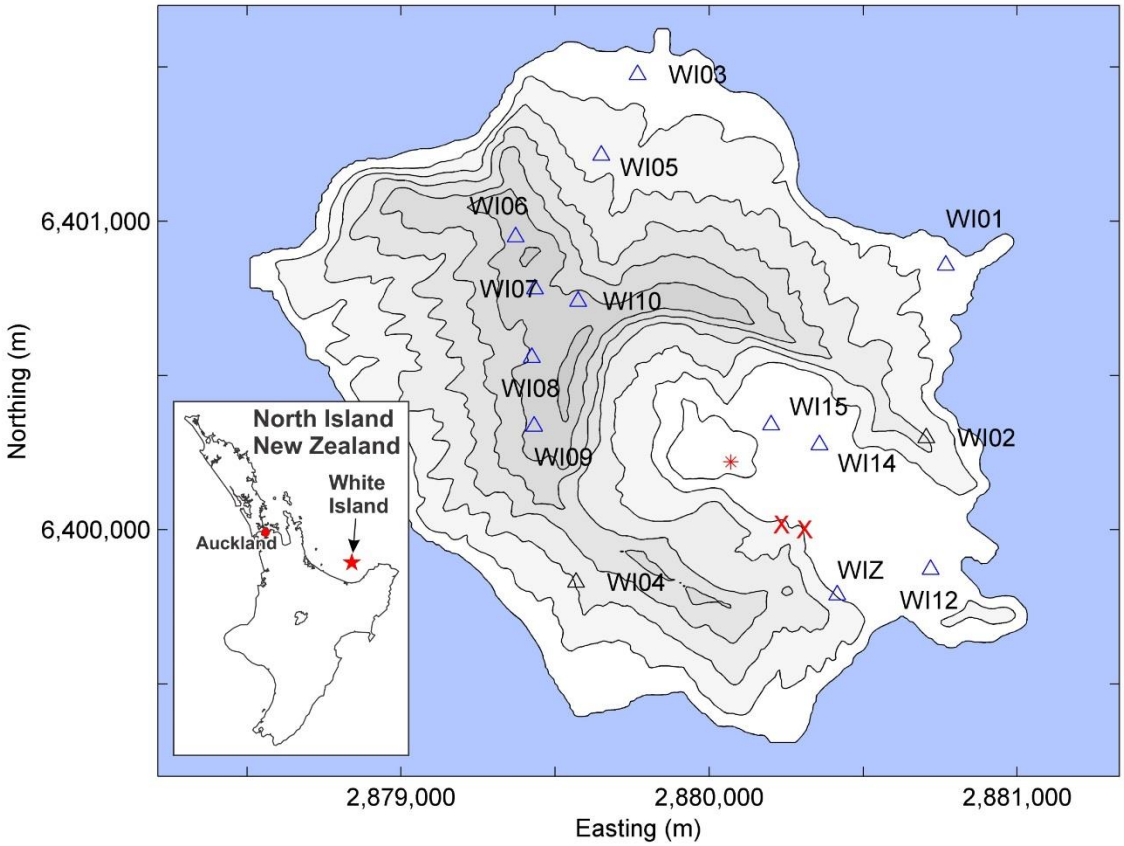

Fig 1: Map showing White Island with location of permanent seismic station (WIZ) and temporary portable seismic stations (open blue triangles) deployed in 2011 Stations WI02 and WI04 (black triangles) had issues with horizontal component sensors and hence were not used for the semblance computation. The site of small scale eruptive activity in 2012-2013 is marked by stars while the red X's mark the location of high discharge fumaroles. Contour interval is 50 m.

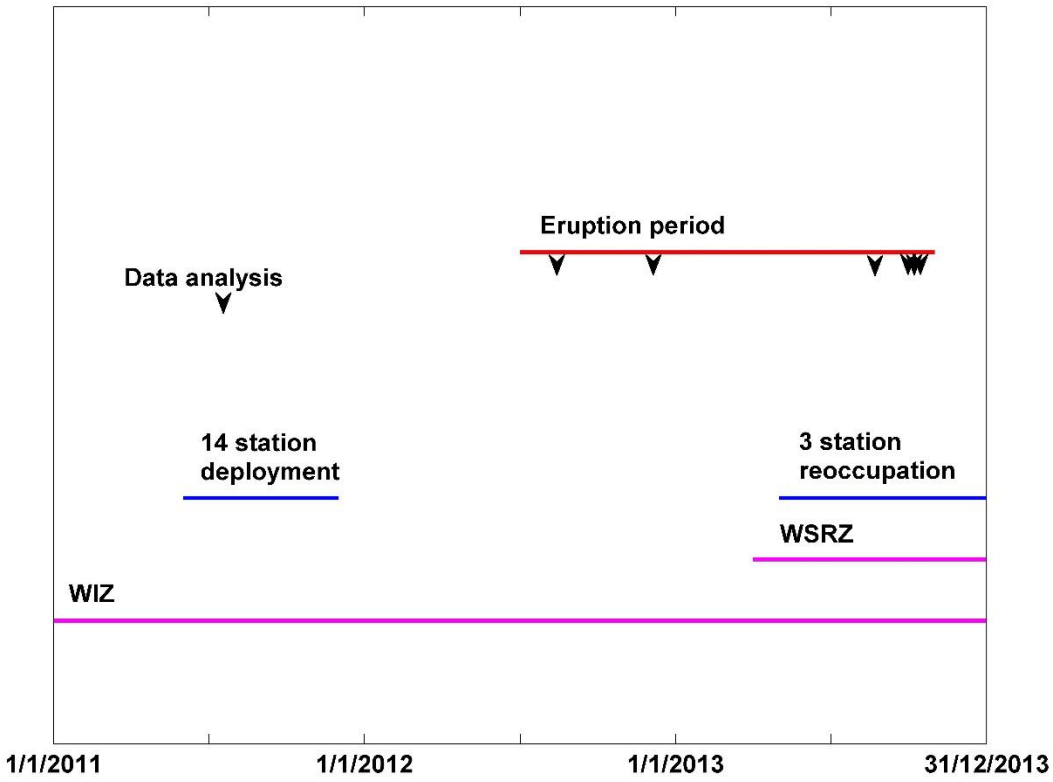

1265

1266 Fig 2: Timeline of volcanic unrest (red line) and individual eruptive events (black arrows).

1267 The analysis presented here is shown by the black arrow including the period of the 14 station

1268 deployment in blue. The permanent station operation is shown in magenta.

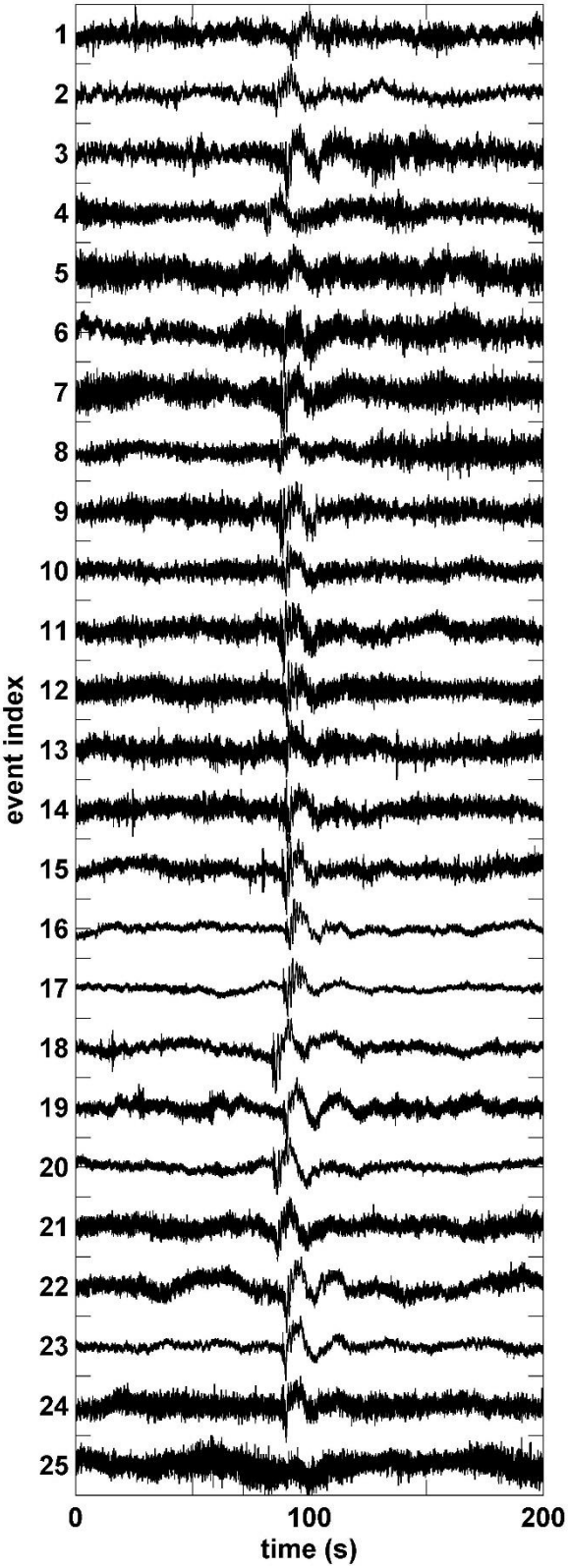
1
2
3
4
5
6
7
8
9
10
11
12
13
14
15
16
17
18
19
20
21
22
23
24
25
event index
0
100
200
time (s)

Fig 3: Unfiltered normalised velocity waveforms for an earthquake swarm occurring 19-21 August 2011 on station WIZ. The events are identified based on their VLP signal but also include variable long period and high frequency components.

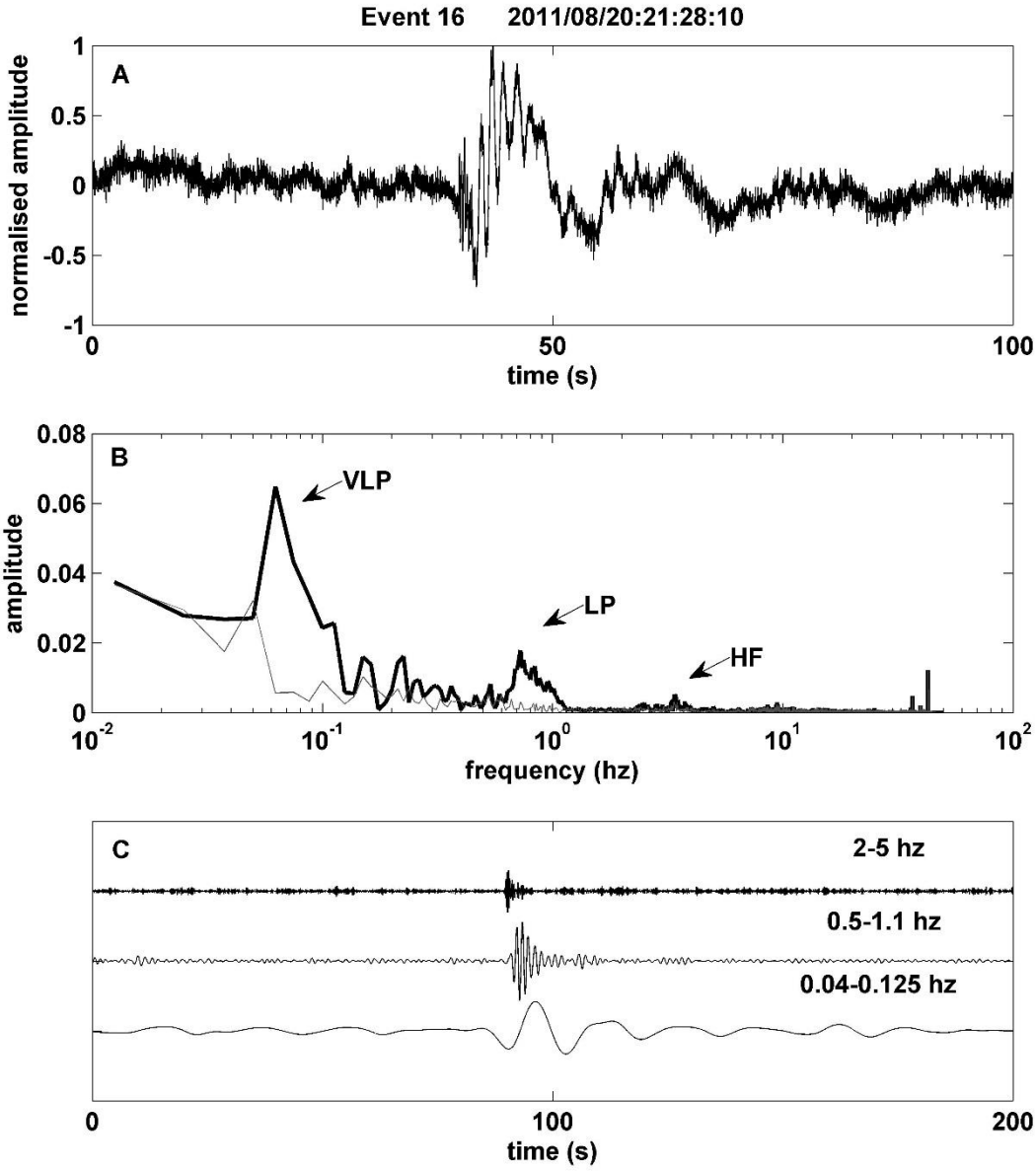

Fig 4: Example waveform and spectra for event 16 showing multi-phase character of the sequence. Panel A shows the raw normalised seismogram, panel B shows the associated spectrum with VLP (0.04-0.125 Hz), LP (0.5-1.1 Hz) and HF (2-5 Hz) components. The

1277 spikes observed at >40 Hz are probably associated with wind-noise. The pre-event noise is

1278 shown as the grey line. Zero-phase filtered seismograms in the selected pass bands are

1279 shown in Panel C.

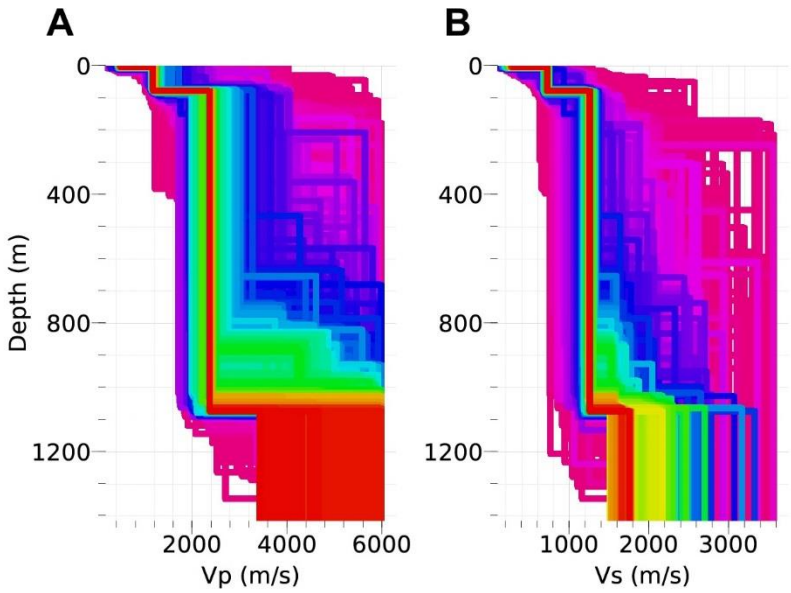

1280

1281 Fig 5: Example inversion of Rayleigh dispersion from the White Island dense array

1282 deployment for V_p (A), V_s (B). Warm colours represent models with lower misfits..

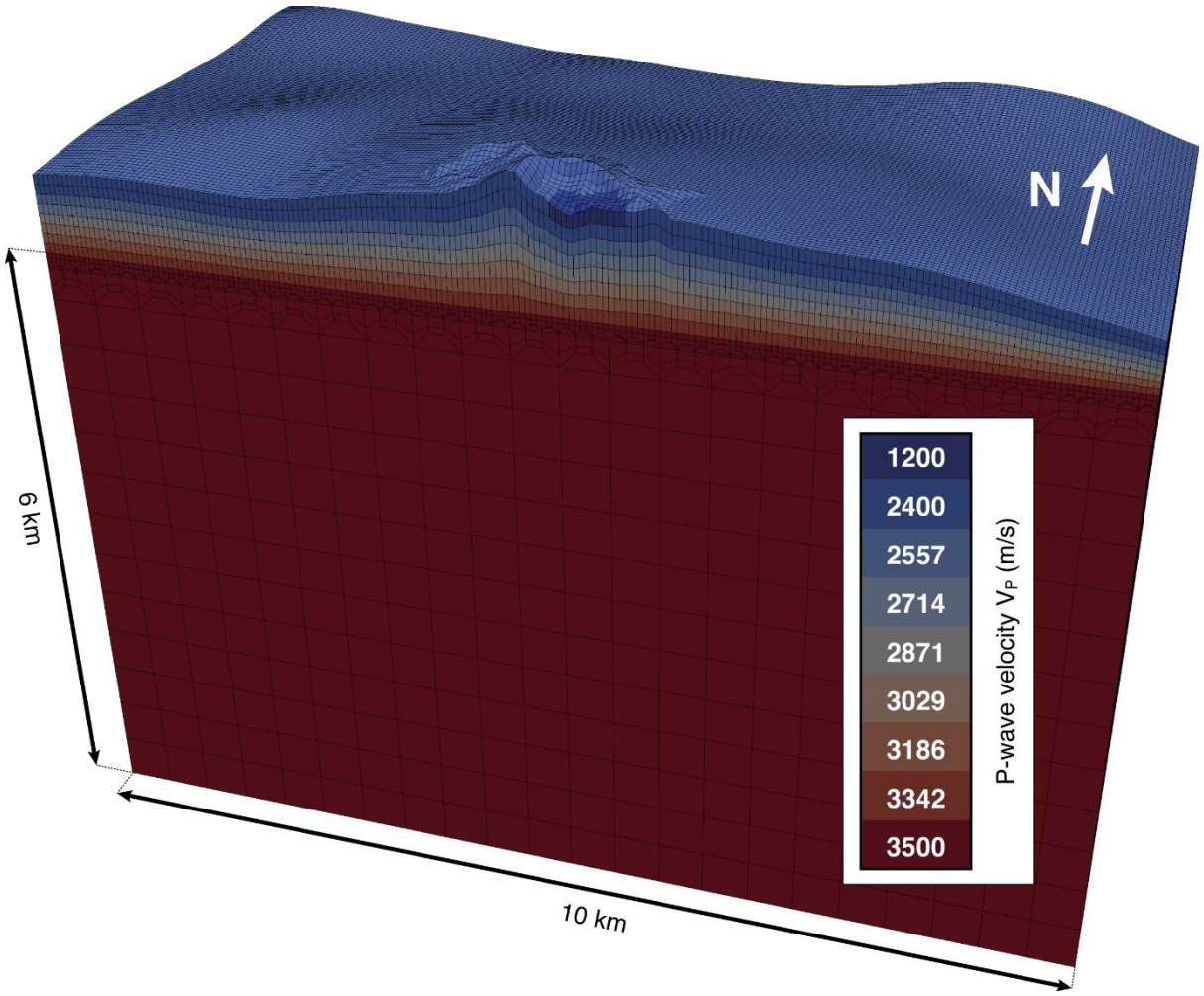

Fig: 6: Sectional view of the computational model used for the numerical calculation of synthetic seismograms. The free surface is modelled after the topography of White Island and its surrounding bathymetry. A homogeneous velocity model (V_P = 2.2 km/s) with otherwise identical model geometry was used for the synthetic test and the HF, LP, and VLP locations as well as the inversion analysis.

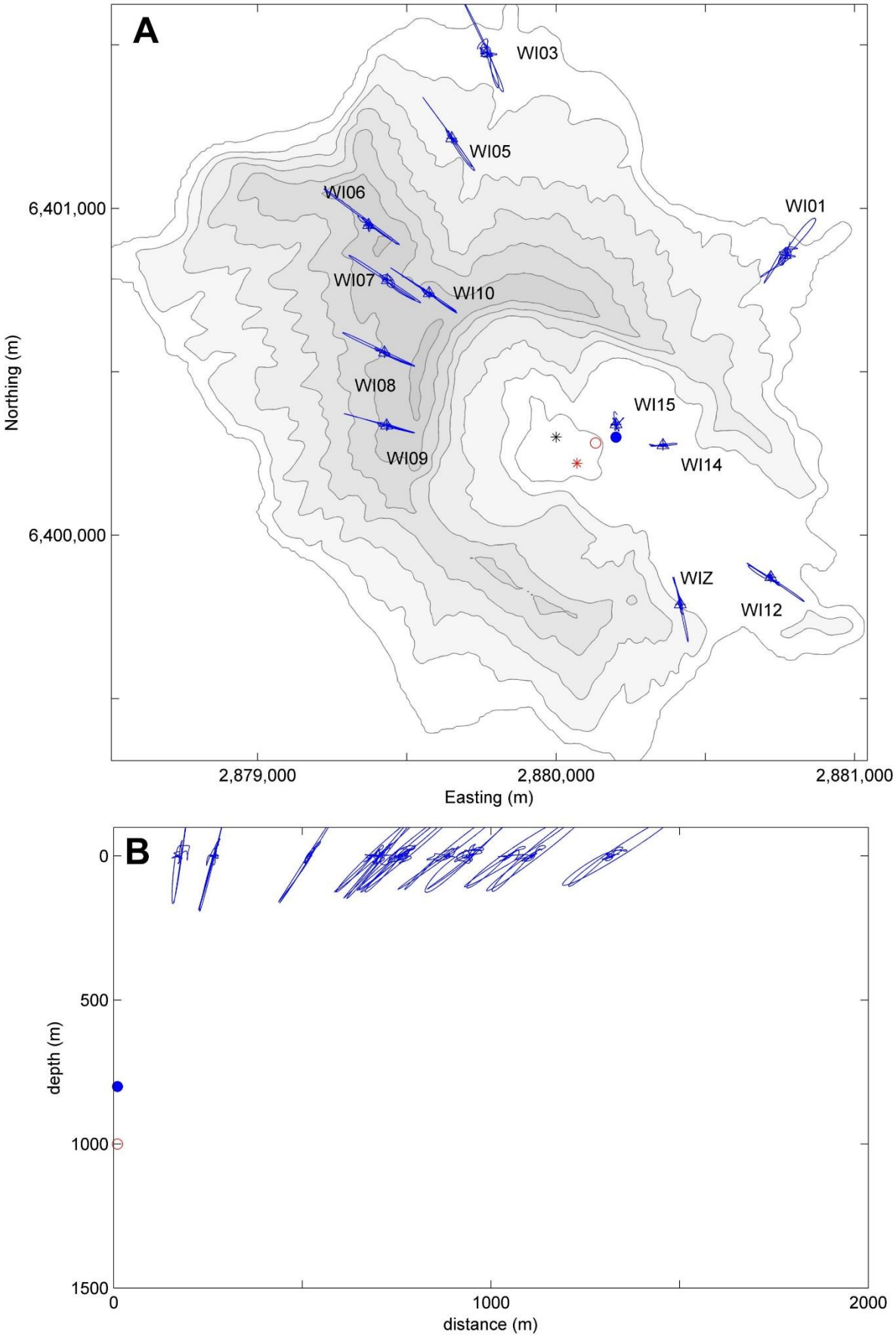
A
WI03
WI05
WI06
WI01
WI07
WI10
WI08
WI15
WI09
WI14
WIZ
WI12
6,401,000
6,400,000
Northing (m)
2,879,000
2,880,000
2,881,000
Easting (m)
B
0
500
1000
1500
depth (m)
0
1000
2000
distance (m)

1291

Fig 7: Map view particle motions (A) for synthetic isotropic source located at 1 km below sea level (Case 1). Synthetics are created using the spectral element method outlined in Section 4.2. The red star is a known eruption vent and the black star is a small dome emplaced in September to November 2012, while the red circle is the location derived for the synthetic seismograms and blue filled circle is the best fit location based on waveform semblance as described in Kawakatsu et al., (2000). Particle motions (B) projected to vertical plain for synthetic seismograms at the best fit location determined from waveform semblance. The best fit location matches closely the location of the synthetic source, validating the waveform semblance codes.

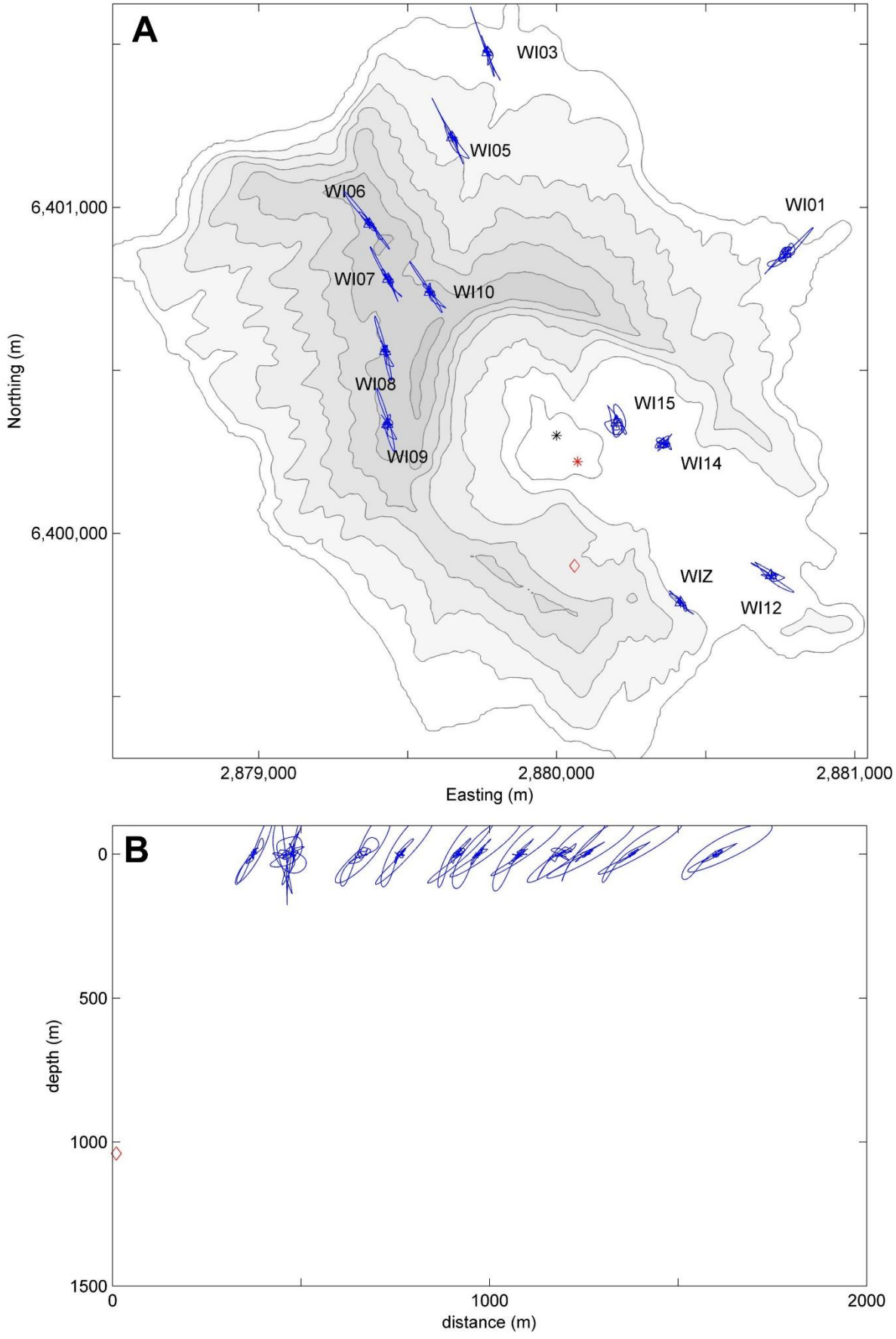
A
WI03
WI05
WI06
WI01
WI07
WI10
WI08
WI15
WI14
WI09
WIZ
WI12
6,401,000
6,400,000
Northing (m)
2,879,000
2,880,000
2,881,000
Easting (m)
B
0
500
1000
1500
depth (m)
0
1000
2000
distance (m)

1301

Fig 8: Map view particle motions (A) for VLP component of event 17. The best fit location is approximately 300 m south of the active vent region. Section view particle motions (B) projected from the best fit location (red diamond) based on waveform semblance. Note the general decrease in slant angle with distance from the inferred source location.

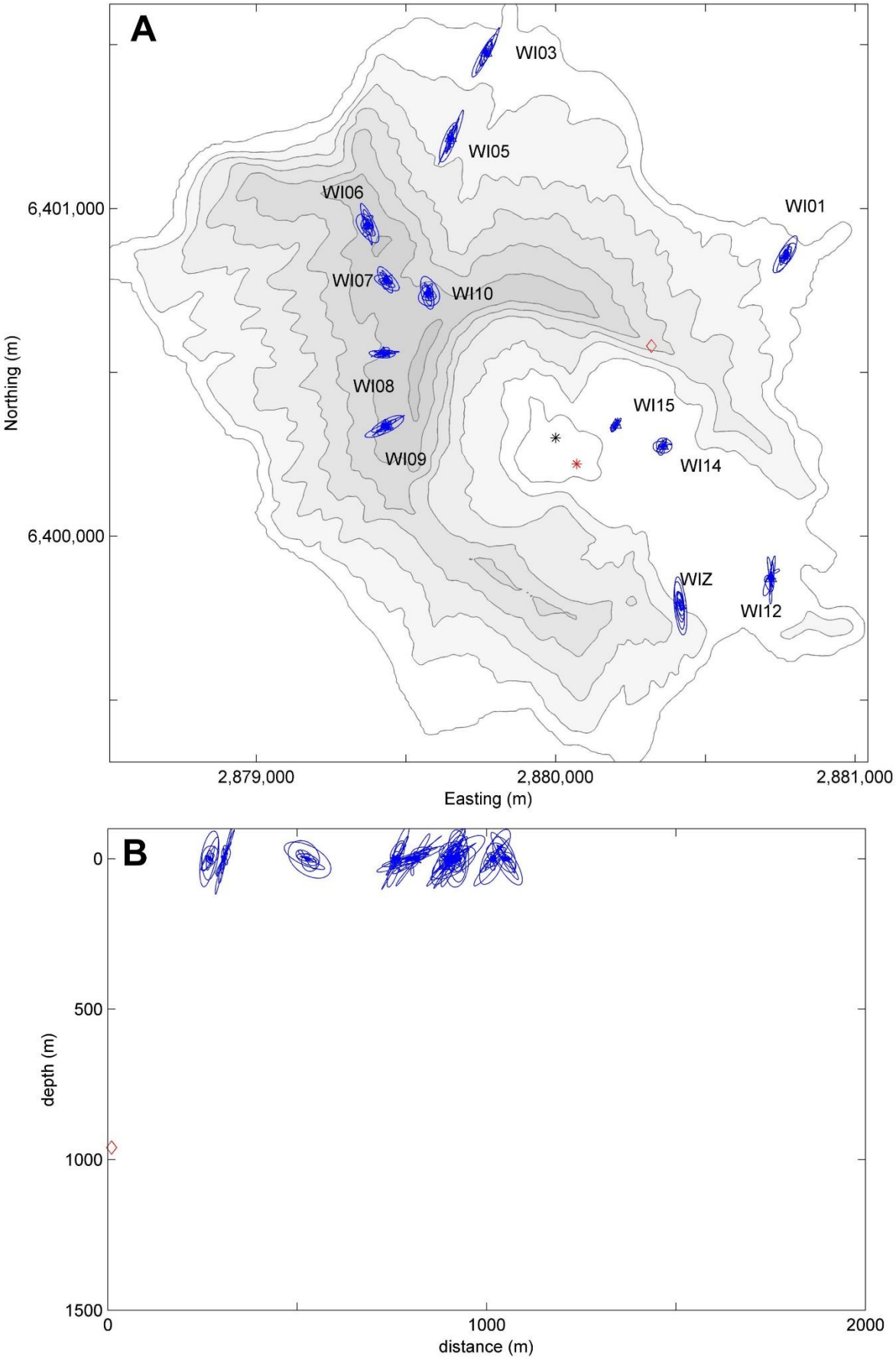
A
WI03
WI05
WI06
WI01
WI07
WI10
WI08
WI15
WI14
WI09
WIZ
WI12
6,401,000
6,400,000
Northing (m)
2,879,000
2,880,000
2,881,000
Easting (m)
B
0
500
1000
1500
depth (m)
0
1000
2000
distance (m)

1306

Fig 9: Map view particle motions (A) for LP component of event 17. The best fit location (red diamond) is approximately 300 m northeast of the active vent region. Section view particle motions (B) projected from the best fit location determined using maximum waveform semblance. Note the poor agreement in particle motions here interpreted as a significant departure from an isotropic source pattern.

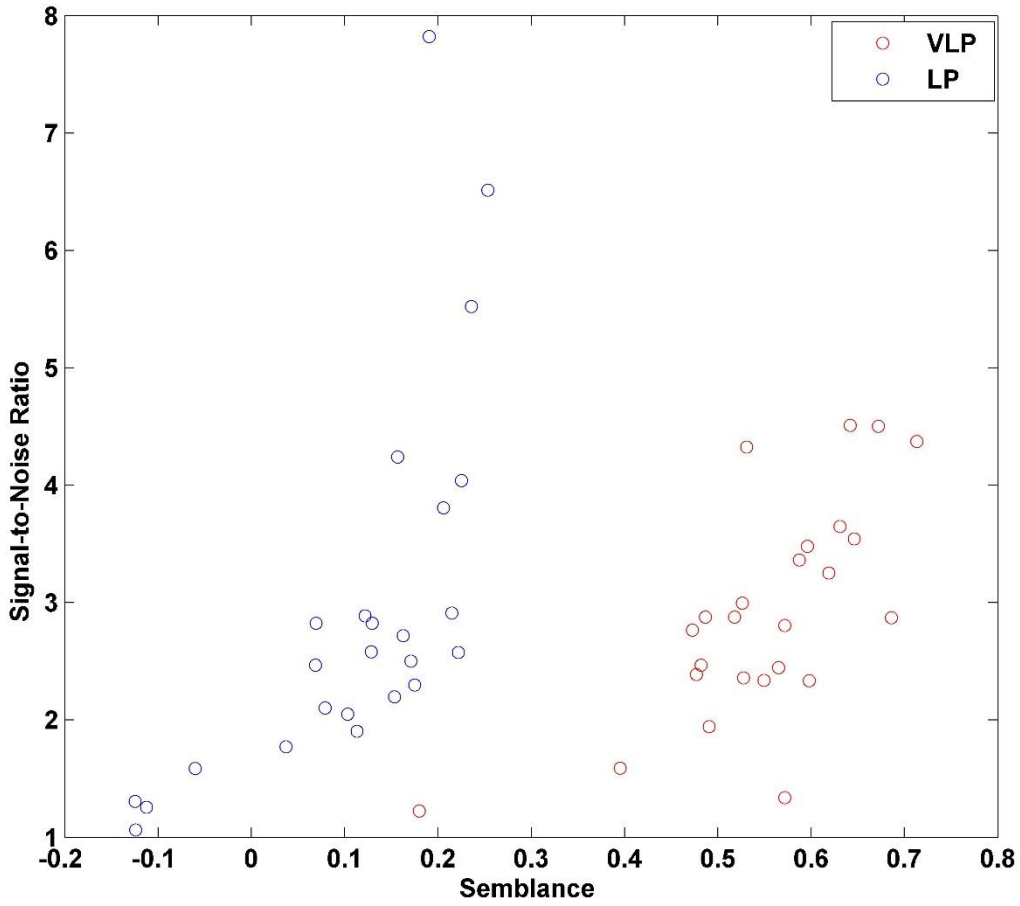

Fig 10: Comparison of signal to noise ratio (SNR) and semblance (see Table 1 and 2) for 25 LP and VLP earthquakes. Signal to noise is computed in the passbands outlined in Fig 3 and are computed for each event compared to the corresponding pre-event noise window. Note strong VLP correlation between SNR and computed semblance for SNR below 3.

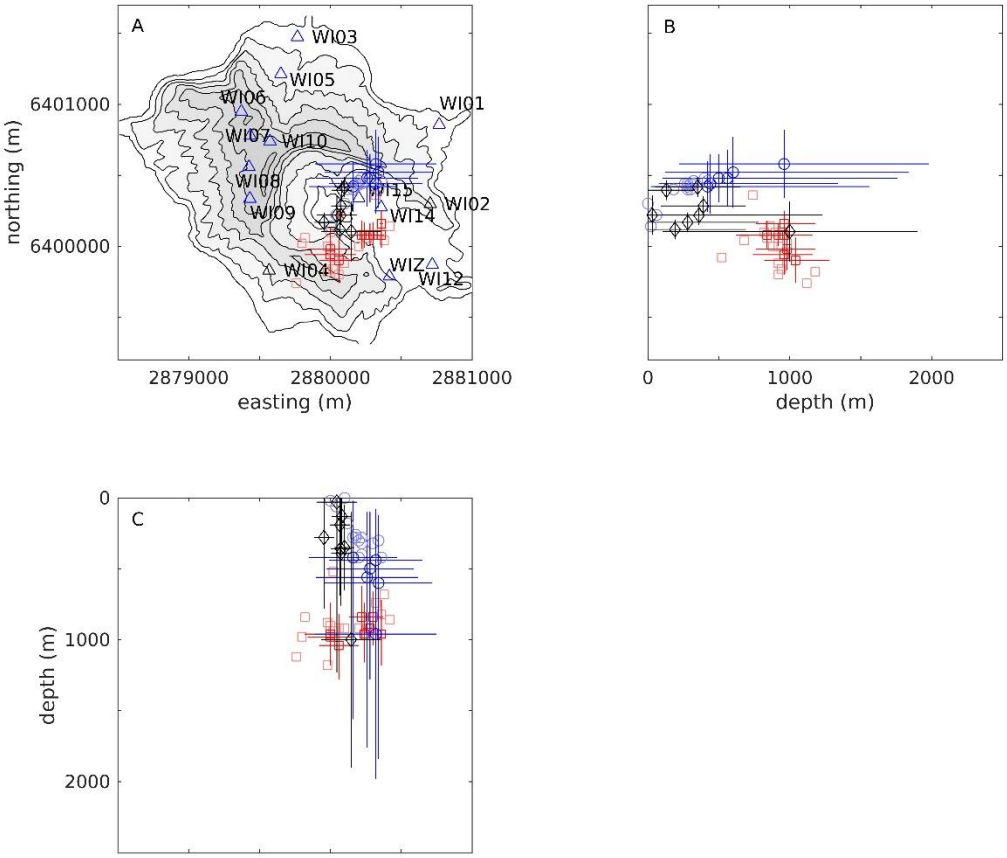

1317

1318 Fig 11: Locations and error bounds for VLP (red), LP (blue) and HF (black) sources. LP and
1319 VLP sources are located using waveform semblance approach outlined in Section 4.1. HF
1320 locations are determined using Hypo71, via triangulation of picked arrival times in the
1321 temporary network. See Table 1 for detailed summary of the results.

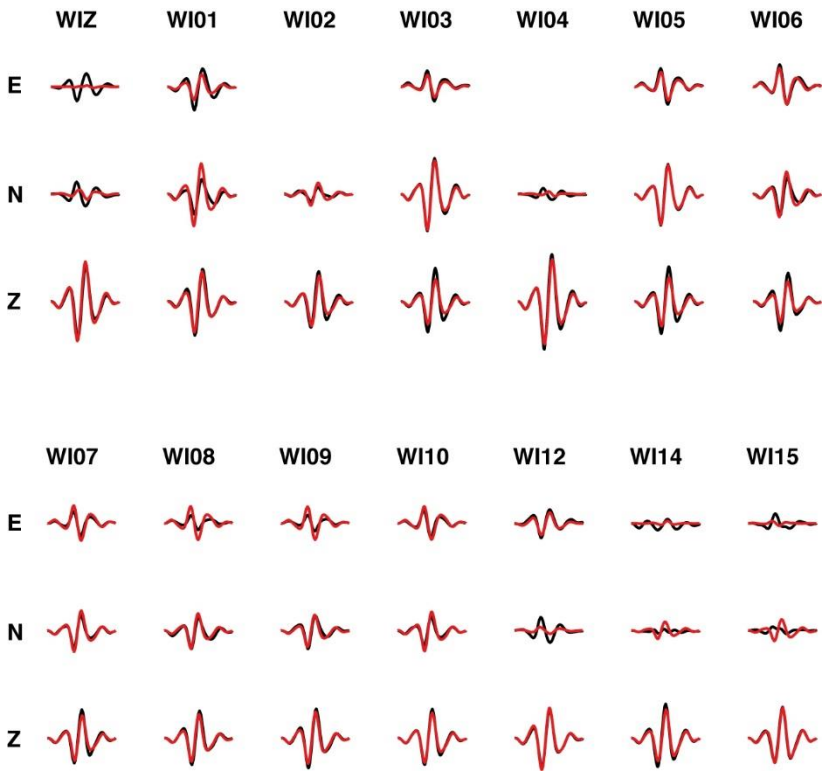

Fig 12 Waveform fit for the moment tensor inversion (MTI) of the VLP stack without single forces. The original seismograms for all stations and components are shown in black, the corresponding synthetic seismograms for the MTI result in red. The faulty East components of the stations WI02 and WI04 which were not used for the inversion are blank. A common scale is used for all seismograms.

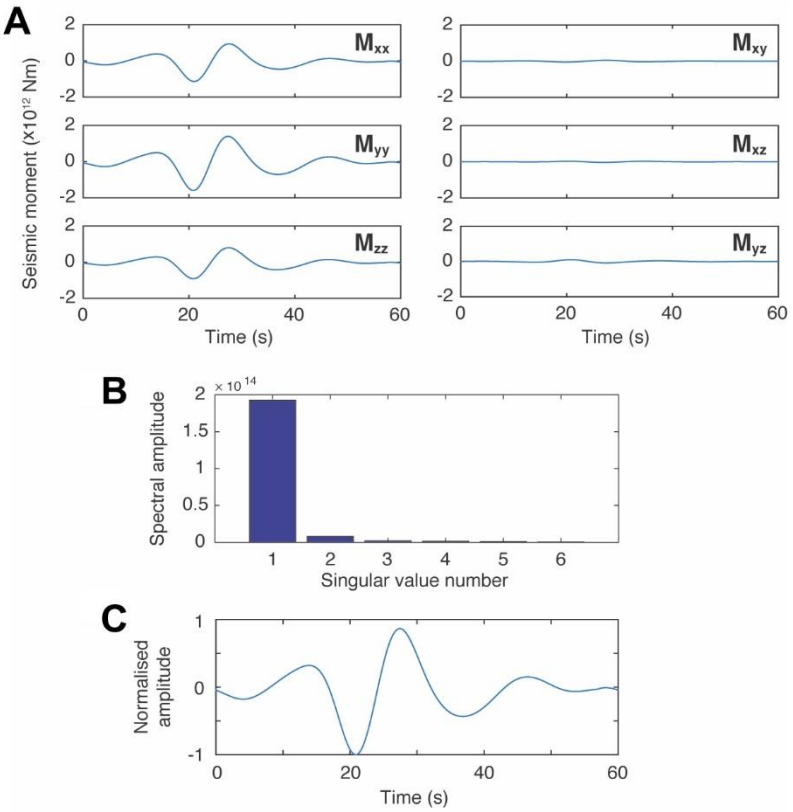

Fig 13 Moment tensor inversion results for the VLP stack. A) Full solutions of all 6 MT components, exhibiting most of the energy on the diagonal elements (left), whereas little energy falls on the off-diagonal components (right). B) Spectral amplitude of the singular values of the Vasco (1989) decomposition, showing that a unique source time function can be found for all MT components (shown in C)). This STF, multiplied with the MT components in Table 4, yields a robust representation of the MTI results.

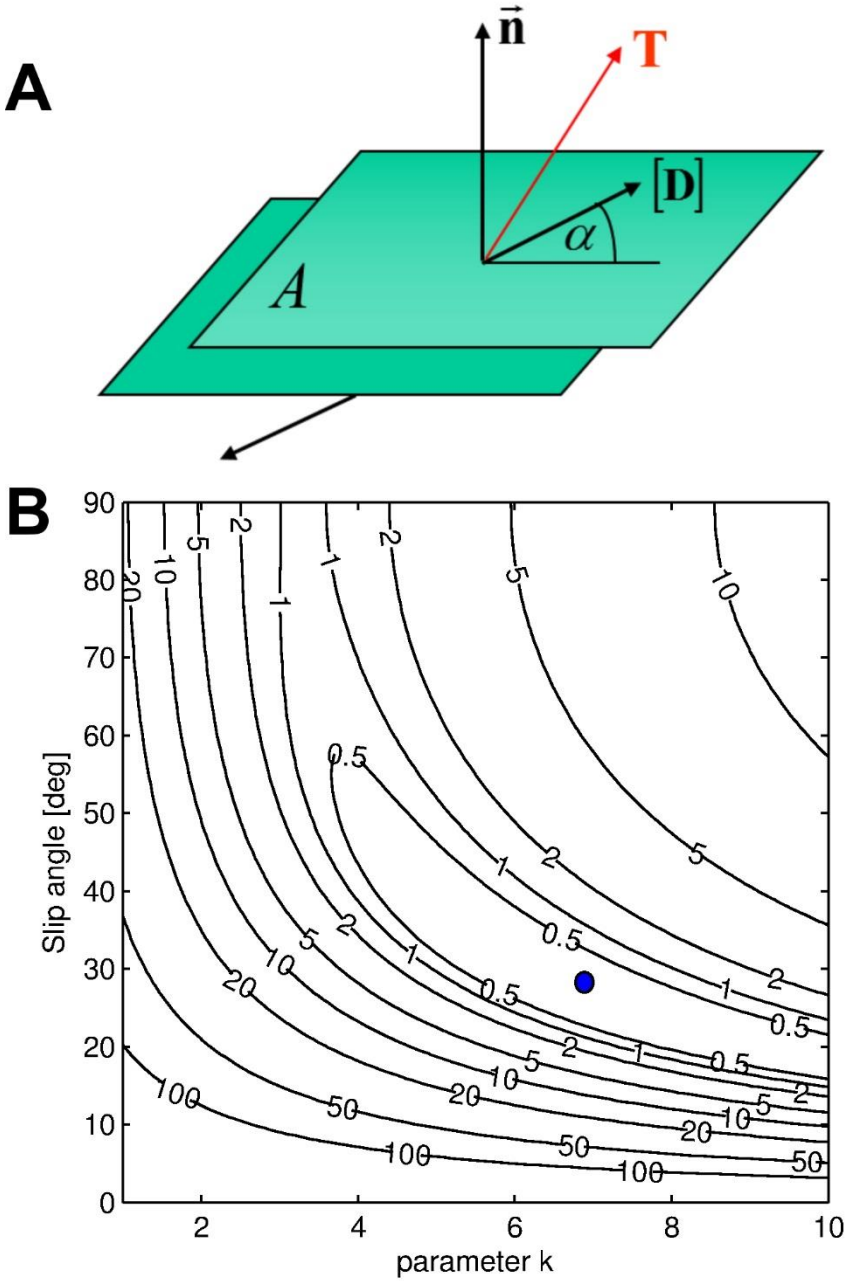

Fig 14 A) A sketch of the tensile earthquake. **D** is the slip vector on the fault and its direction is determined by the angle α from the fault plane. B) Contour plot of R_2 misfit (in percentage) between the theoretical and observed principal values of moment-tensor for a general non-DC crack source. The blue solid circle denotes the minimum misfit. However, the whole region is within the 1% misfit range and can be considered as viable candidates for the source mechanism.

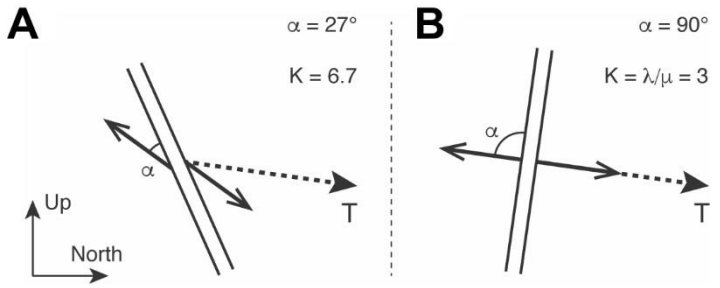

Fig 15. Illustration of the VLP source mechanism. A) The best solution suggests a quasi-vertical tensile crack with a significant amount of shear movement. B) An alternative solution, also with a relatively low residual. The examples illustrate our inability to robustly resolve between the different mechanisms.

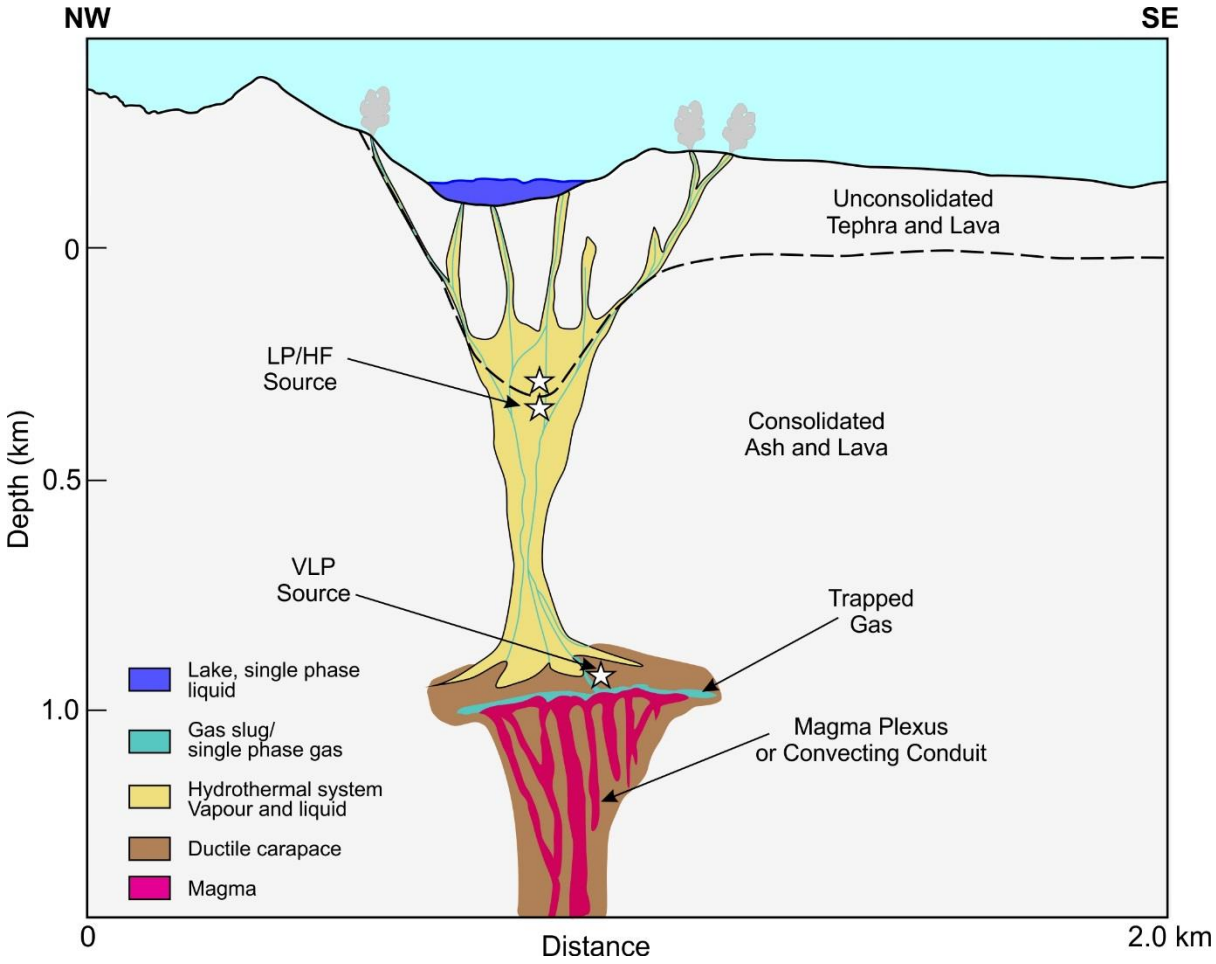

Fig 16 Conceptual model of coupled VLP/LP/HF source processes. VLP source is inferred to be at the top of the magma carapace at ~1 km depth. Gas slug release propagates to shallow depths inducing failure of unconsolidated ash and lava materials in the vent or vent walls (Heap et al, 2016). Alternatively, the shallow hydrothermal/vent fill system may include strong cavity resonance characteristics that may generate LP (e.g., Chouet 1996; Neuberg et al, 2002). Localised HF seismicity may result from failure due to stress concentration near to a localised conduit constriction.

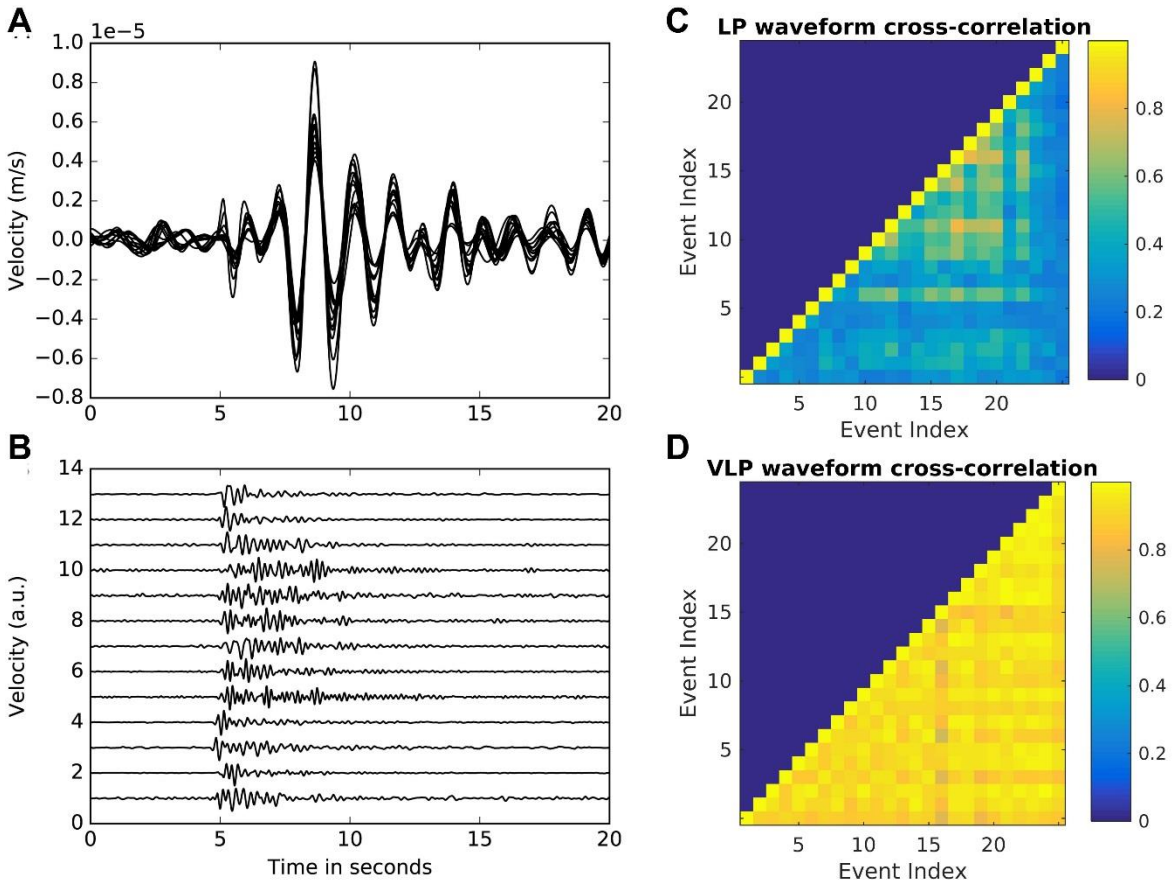

Fig 17: A) Vertical LP waveforms (event 11, filtered between 0.4 and 1.2 Hz) aligned for all stations maximising the cross-correlation between all trace pairs. Station WI04 was omitted due to a considerably different waveform. B) The same traces filtered between 0.4 and 5 Hz and plotted individually. Note that the HF waveforms are incoherent between stations and their onset time relative to the LP vary by a few tenths of a second. This suggests that HF

and LP signals originate at slightly different locations. C) waveform cross-correlation matrix for LP earthquakes, D) equivalent cross-correlation matrix for VLP events.